SANDIA REPORT
SAND2014-1153
Unlimited Release
Printed February 2014

Transport-reaction model for defect and carrier behavior within displacement cascades in gallium arsenide

William R. Wampler and Samuel M. Myers

Prepared by
Sandia National Laboratories
Albuquerque, New Mexico 87185 and Livermore, California 94550

Sandia National Laboratories is a multi-program laboratory managed and operated by Sandia Corporation, a wholly owned subsidiary of Lockheed Martin Corporation, for the U.S. Department of Energy's National Nuclear Security Administration under contract DE-AC04-94AL85000.

Approved for public release; further dissemination unlimited.

Sandia National Laboratories

Issued by Sandia National Laboratories, operated for the United States Department of Energy by Sandia Corporation.

NOTICE: This report was prepared as an account of work sponsored by an agency of the United States Government. Neither the United States Government, nor any agency thereof, nor any of their employees, nor any of their contractors, subcontractors, or their employees, make any warranty, express or implied, or assume any legal liability or responsibility for the accuracy, completeness, or usefulness of any information, apparatus, product, or process disclosed, or represent that its use would not infringe privately owned rights. Reference herein to any specific commercial product, process, or service by trade name, trademark, manufacturer, or otherwise, does not necessarily constitute or imply its endorsement, recommendation, or favoring by the United States Government, any agency thereof, or any of their contractors or subcontractors. The views and opinions expressed herein do not necessarily state or reflect those of the United States Government, any agency thereof, or any of their contractors.

Printed in the United States of America. This report has been reproduced directly from the best available copy.

Available to DOE and DOE contractors from
U.S. Department of Energy
Office of Scientific and Technical Information
P.O. Box 62
Oak Ridge, TN 37831

Telephone: (865) 576-8401
Facsimile: (865) 576-5728
E-Mail: reports@adonis.osti.gov
Online ordering: http://www.osti.gov/bridge

Available to the public from
U.S. Department of Commerce
National Technical Information Service
5285 Port Royal Rd.
Springfield, VA 22161

Telephone: (800) 553-6847
Facsimile: (703) 605-6900
E-Mail: orders@ntis.fedworld.gov
Online order: http://www.ntis.gov/help/ordermethods.asp?loc=7-4-0#online

SAND2014-1153
Unlimited Release
Printed February 2014

Transport-reaction model for defect and carrier behavior within displacement cascades in gallium arsenide

William R. Wampler
Radiation-Solid Interactions Department 1111
Sandia National Laboratories
P.O. Box 5800
Albuquerque, New Mexico 87185-MS1056

Samuel M. Myers
S. M. Myers Consulting,
Albuquerque, NM

Abstract

A model is presented for recombination of charge carriers at displacement damage in gallium arsenide, which includes clustering of the defects in atomic displacement cascades produced by neutron or ion irradiation. The carrier recombination model is based on an atomistic description of capture and emission of carriers by the defects with time evolution resulting from the migration and reaction of the defects. The physics and equations on which the model is based are presented, along with details of the numerical methods used for their solution. The model uses a continuum description of diffusion, field-drift and reaction of carriers and defects within a representative spherically symmetric cluster. The initial radial defect profiles within the cluster were chosen through pair-correlation-function analysis of the spatial distribution of defects obtained from the binary-collision code MARLOWE, using recoil energies for fission neutrons. Charging of the defects can produce high electric fields within the cluster which may influence transport and reaction of carriers and defects, and which may enhance carrier recombination through band-to-trap tunneling. Properties of the defects are discussed and values for their parameters are given, many of which were obtained from density functional theory. The model provides a basis for predicting the transient response of III-V heterojunction bipolar transistors to pulsed neutron irradiation.

ACKNOWLEDGMENTS

The authors thank Alan Wright and Peter Schultz for their extensive calculations of properties of defects in GaAs using DFT, especially for formation energies and reaction networks by Peter Schultz and pathways and energy barriers for migration by Alan Wright. The authors acknowledge valuable contributions from Philip Cooper in providing defect maps for neutron irradiated GaAs, and from Stephen Foiles for Molecular Dynamics simulations of collision cascades in GaAs, which together were used to determine a representative radial defect concentration profile for neutron damage. The authors thank Don King, Edward Bielejec and George Vizkelethy for providing the measurements of transient gain in Npn HBTs after pulsed ion irradiation. The authors acknowledge valuable discussions with David Lang, Andreas Schenk and Normand Modine on the topic of field-enhanced carrier capture. The authors also thank Robert Fleming for providing data from his DLTS experiments prior to publication, and for the corresponding parameter values for field-enhanced carrier emission. This work was conducted at Sandia National Laboratories under the auspices of the U.S. Department of Energy's National Nuclear Security Administration.

Sandia National Laboratories is a multi-program laboratory managed and operated by Sandia Corporation, a wholly owned subsidiary of Lockheed Martin Corporation, for the U.S. Department of Energy's National Nuclear Security Administration under contract DE-AC04-94AL85000.

CONTENTS

Acknowledgments 4

Contents 5

1. Introduction 7

2. Description of the model 9
   2.1. Collision cascades 9
   2.2. Transport 10
   2.3. Reactions 12
      2.3.1. Carrier reactions 12
      2.3.2. Field-enhanced carrier capture and emission by tunneling 14
      2.3.3. Reactions among defects and dopants 16

3. Defect species and reactions included in the model 18

4. Methods of solution 22
   4.1. Flux equation 22
   4.2. Poisson's equation 23
   4.3. Carrier capture and emission reactions 25
   4.4. Evaluation of inverse Fermi integral 25
   4.5. Boundary conditions 26
   4.6. Initial conditions 27
   4.7. Verification 27

5. Simulations 28

6. Effect of field-enhanced band to trap tunneling on carrier recombination 31

7. Conclusion 32

References 34

Tables 37

Figures 40

Distribution 50

1. INTRODUCTION

This report describes a new computational model for simulation of recombination of charge carriers at evolving displacement damage in III-V semiconductor materials produced by neutron or ion irradiation. This model provides a microscopic description of the transport and reaction of charge carriers and defects within the atomic displacement cascade produced by an energetic collision event. The principal reactions of mobile defects and carriers are treated, in the continuum approximation, for a statistically representative defect cluster. The intent is to include this microscopic recombination model as a carrier sink term in macroscopic models of carrier flow within devices such as heterojunction bipolar transistors (HBTs). In such simulations, the device model gives the local carrier concentrations, which provide boundary conditions for calculations of carrier recombination at damage cascades at various locations within the device. Simulations of carrier recombination within defect clusters provide the device model with the net local carrier recombination rate, which varies with time and position within the device. This approach is intended to provide a higher fidelity description of carrier recombination than the empirical recombination model presently used by the Sandia program on Qualification Alternatives to the Sandia Pulsed Reactor (QASPR) to simulate the transient response of HBTs to pulsed neutron irradiation. This report describes the model for carrier recombination within a defect cluster, but does not include incorporation of this recombination model into a device model.

Here we describe an implementation of this recombination model for gallium arsenide (GaAs), the material used in the base and collector of Npn HBTs produced at Sandia. The notation Npn denotes n-type emitter, p-type base and n-type collector and the upper case N denotes wider band gap material in the emitter. A similar model was previously developed for silicon [1]. Such an atomistic model is far more challenging for GaAs than for silicon, because the defect physics is more complex and less well understood. However, recent theoretical work using density functional theory, has greatly improved knowledge of defects in GaAs. This new information on defect properties provides a technical basis for extending the atomistic model to GaAs.

The motivation for developing an atomistic model for carrier recombination is that by including more detailed descriptions of physical processes, the model will have broader range of application and less reliance on calibration than simpler empirical models. However, defect behavior is complex and such modeling cannot provide accurately quantitative predictions based solely on independently available parameter values. The uncertainties in a number of key quantities are too large for this, and in addition the calculations entail a variety of simplifying approximations. Therefore, the objective is a mechanistic description that captures important features and trends and that ultimately can be made consistently quantitative through refinement of parameter values within physically reasonable bounds. The approach involves identification of important physical processes and formulation of corresponding equations and numerical methods for their solution. Model development includes verification that the code is correctly solving the equations, which is done by running simulations designed to test various functionalities of the code for which analytical solutions are available. Finally, the code must be compared to available experimental information to determine whether the physics and approximations are adequate.

This paper is organized as follows. Section II gives the equations describing transport and reaction of carriers and mobile defects on which the model is based. Section II also includes a discussion of field-enhanced carrier capture by band-to-trap tunneling. Section III describes the defect species included in the model and gives values for their properties, including formation and migration energies which were obtained from density functional theory (DFT) simulations. Section IV describes numerical methods used to solve the equations. Section V presents results from simulations for conditions relevant to carrier recombination in an HBT.

2. DESCRIPTION OF THE MODEL

2.1. Collision cascades

Energetic recoils from neutron collision events produce atomic displacement cascades with defects spatially localized in clusters. This clustering of the defects has profound effects on carrier recombination and defect annealing and is therefore a central feature of the model. Although neutron or ion irradiation produces collision cascades that vary greatly in size and structure, the clustering is approximated in the model as a single, representative, radially symmetric cluster. The initial radial distributions of defects within this cluster are obtained from a pair correlation function analysis [1] of defect maps from a large number of recoil events calculated using the binary collision code Marlowe [2] for a distribution of recoil energies corresponding to a desired irradiation condition. The first stage of this analysis evaluates pair autocorrelation functions for the primal defects surviving spontaneous recombination, which reflect the statistically averaged surroundings of an individual defect. Defect concentration profiles for use in the modeling are then constructed so as to yield the same correlation functions as the defect map, thereby capturing to first order the variation in local defect environments. While this approximation is a considerable simplification of a complex reality, the disparity is lessened by subcascade formation at higher recoil energies, which makes the effective range of cluster sizes less extreme. The fidelity of the result is believed sufficient to describe important features and trends. Such a correlation-function approach is fully objective, avoiding subjective choices relating to the definitions of a cluster and its center.

Another significant approximation in the model is that the collision cascade is treated as a collection of point defects, whose properties, such as energies of formation and migration, are not influenced by neighboring defects. Thus, defect and carrier reactions in the central core region and in the lower concentration outer regions of the cluster are treated in the same way. In reality, the concentration of defects in the core is so high that this approximation may break down. Molecular dynamics simulations show that the lattice structure in the core region may be disordered or amorphous-like [3]. Electronic properties of small dense defect clusters have been examined by density functional theory in GaAs [4] and Si [5]. These were found to have many electronic states and energy levels in the band gap and thus should contribute to carrier recombination. However, the contribution of the high-density core to overall carrier recombination can be limited by carrier transport into this region, in which case atomistic details

are less influential. The significance of this approximation thus depends qualitatively on which process is rate determining.

2.2. Transport

Continuity equations specify the rate of change of concentration n_i for the various species i being followed, which include conduction electrons, holes, dopants and defects in their various charge states. For spherical geometry these equations are of the form:

$$\frac{\partial n^i}{\partial t} = -\frac{1}{x^2}\frac{\partial}{\partial x}\left(x^2\Phi^i\right) + reaction\ terms \qquad (1)$$

where x is the radius. The reaction terms give the rate of removal or creation of species i through reactions with other species such as carrier capture/emission or defect reactions.

The flux of charge carriers can be expressed in terms of a gradient of the chemical potential ψ:

$$\Phi = -\frac{\mu n}{e}\frac{d\psi}{dx} \qquad (2)$$

where e is the elementary unit of charge, and the mobility

$$\mu = \left|\frac{v_{drift}}{F}\right|$$

is defined in terms of a drift velocity, v_{drift} in an electric field F.

For electrons and holes, the spatially dependent part of the chemical potential depends on the local electrostatic potential V, and a concentration dependent term ψ_c :

$$\psi^e = -eV + \psi_c^e \quad \text{for electrons, and} \qquad (3)$$

$$\psi^h = eV + \psi_c^h \quad \text{for holes,}$$

where the ψ_c are expressed relative to the corresponding band edge. The conduction electron chemical potential corresponds to the electron quasi-Fermi level within an additive constant. The hole chemical potential corresponds to the negative of the hole quasi-Fermi level within an additive constant.

When the concentration of electrons or holes is small compared to the density of states N_C for the conduction band and N_V for the valence band, Boltzmann statistics apply and ψ_c can be approximated as:

$$\psi_c^e = kT\, ln\left(\frac{n^e}{N_C}\right) \text{ for electrons, and} \tag{4}$$

$$\psi_c^h = kT\, ln\left(\frac{n^h}{N_V}\right) \text{ for holes,}$$

where k is Boltzmann's constant and T is the temperature. In this case equation 2 takes the familiar form

$$\Phi^e = -n^e\, \mu F - \mathrm{D}\, \frac{\partial n^e}{\partial x} \text{ for electrons} \tag{5}$$

and

$$\Phi^h = n^h\, \mu F - \mathrm{D}\, \frac{\partial n^h}{\partial x} \text{ for holes.}$$

Here we use a generalized form of the Einstein relation between diffusivity D and mobility μ for species with multiple charge q=Qe, where e is the elementary charge and Q is the charge state:

$$D = \left(\frac{kT}{|q|}\right)\mu\ . \tag{6}$$

When carrier concentrations are not small compared to the density of states, the carrier chemical potential is given by

$$\psi_c^e \equiv kT\, \mathcal{F}_{1/2}^{-1}\left(\frac{n^e}{N_C}\right) \text{ for electrons, and} \tag{7}$$

$$\psi_c^h \equiv kT\, \mathcal{F}_{1/2}^{-1}\left(\frac{n^h}{N_V}\right) \text{ for holes,}$$

where $\mathcal{F}_{1/2}^{-1}$ is the inverse function of the Fermi-Dirac integral for a parabolic band,

$$\mathcal{F}_{1/2}(u) = \frac{2}{\sqrt{\pi}}\int_0^\infty \frac{x^{1/2}}{1+\exp(x-u)}\, dx \tag{8}$$

and equations 4 and 5 no longer apply.

For mobile defects Boltzmann statistics apply. This results in an analog to equation 5 for the flux where mobility is replaced by the diffusivity using equation 6 including the charge q of the defect.

$$\Phi = \mathrm{D}\left(\mathrm{n}\, \frac{qF}{kT} - \frac{\partial \mathrm{n}}{\partial x}\right). \tag{9}$$

The electric potential V is determined from the charge density ρ by solving Poisson's equation, which for spherical geometry is:

$$\frac{1}{x^2}\frac{d}{dx}\left(x^2\, \frac{dV}{dx}\right) = -\frac{\rho}{\varepsilon} \tag{10}$$

where ε is the dielectric constant of the material.

The dependence of carrier mobility on electric field strength |F| is calculated from:

$$\mu_h = \frac{\mu_0}{1 + \frac{\mu_0 |F|}{v_{sat}}} \tag{11}$$

for holes, where μ_o is the mobility at low field and v_{sat} is the saturation velocity at high field [6]. For electrons in GaAs the field dependence of mobility is calculated from

$$\mu_e = \frac{\left(\mu_0 + \frac{v_{sat}}{|F|}\left(\frac{F}{F_0}\right)^4\right)}{1 + \left(\frac{F}{F_0}\right)^4} \tag{12}$$

to include the transferred electron effect, where F_0 is a saturation field strength [7]. The low field mobilities are input parameters whose value depends on doping concentration and temperature.

2.3. Reactions

2.3.1. Carrier reactions

The reaction terms in equation 1 remove or create carriers and defect species. Reactions involving charge carriers are treated as reversible and are formulated to give correct thermodynamic equilibrium in detailed balance. The electron-hole reactions included are direct recombination and Auger recombination:

$$U\{e,h\} = A\left(n^e n^h - \left(n^e n^h\right)_0\right) + B_e n^e\left(n^e n^h - \left(n^e n^h\right)_0\right) + B_h n^h\left(n^e n^h - \left(n^e n^h\right)_0\right), \tag{13}$$

where A is the coefficient for direct recombination and B_e and B_h are coefficients for Auger recombination. The factor $(n^e n^h)_0$ is the product of electron and hole concentrations in thermal equilibrium under the constraint of constant local charge density.

Reactions in which a defect captures or emits a carrier are of the form illustrated below for the electron capture/emission reaction

$$e + Z_Q \Leftrightarrow Z_{Q-1} + \Delta E^e(Z_{Q-1}); \tag{14}$$

in the forward or exothermic direction, a conduction electron is captured by a defect of type Z in charge state Q, while in the inverse reaction an electron is emitted from a defect of type Z in

charge state Q-1. $\Delta E^e(Z_{Q-1})$ is the positive difference in energy between the initial and final states, also equal to the energy to emit an electron from defect Z_{Q-1} to the conduction band. This can be expressed in terms of defect formation energies as:

$$\Delta E^e(Z_{Q-1}) = E_g - [E_f(Z_{Q-1}) - E_{f0}(Z_Q)] \tag{15}$$

where $E_{f0}(Z_Q)$ and $E_{f0}(Z_{Q-1})$ are the formation energies, referenced to the valence band edge, of the defect in the two charge states in their local minimum energy configuration, and E_g is the band gap energy. The rate equation for the above reaction is:

$$U\{Z_Q, e\} = v_{th}^e \sigma_{Z_Q}^e \left[n^e [Z_Q] - N_C [Z_{Q-1}] exp\left(-\frac{\Delta E^e(Z_{Q-1})}{kT} \right) \right] \tag{16}$$

for Boltzmann carrier statistics, and

$$U\{Z_Q, e\} = v_{th}^e \sigma_{Z_Q}^e n^e \left[[Z_Q] - [Z_{Q-1}] exp\left(-\frac{\left(\psi_f^e + \Delta E^e(Z_{Q-1})\right)}{kT} \right) \right] \tag{17}$$

for Fermi-Dirac carrier statistics. We use the notation U{X,Y} to denote the rate of reaction between species X and Y. n_e , $[Z_Q]$ and $[Z_{Q-1}]$ are the concentrations of the three species involved, v_{th}^e is the electron thermal velocity, $\sigma_{Z_Q}^e$ is the cross section for capture of an electron by defect Z_Q.

The corresponding reaction equations for hole capture and emission are:

$$h + Z_Q \Leftrightarrow Z_{Q+1} + \Delta E^h(Z_{Q+1}) \tag{18}$$

where $\Delta E^h(Z_{Q+1})$ is the energy to emit a hole from defect Z_{Q+1} to the valence band,

$$U\{Z_Q, h\} = v_{th}^h \sigma_{Z_Q}^h \left[n^h [Z_Q] - N_V [Z_{Q+1}] exp\left(-\frac{\Delta E^h(Z_{Q+1})}{kT} \right) \right] \tag{19}$$

for Boltzmann carrier statistics, and

$$U\{Z_Q, h\} = v_{th}^h \sigma_{Z_Q}^h n^h \left[[Z_Q] - [Z_{Q+1}] exp\left(-\frac{\left(\psi_f^h + \Delta E^h(Z_{Q+1})\right)}{kT} \right) \right] \tag{20}$$

for Fermi-Dirac carrier statistics. Note that $\Delta E^h(Z_{Q+1}) + \Delta E^e(Z_Q) = E_g$.

Although equations 17 and 20 correctly describe the behavior for all carrier concentrations >0, computational considerations make it advantageous to evaluate the reaction

rates using equations 16 and 19 when the carrier concentration is small relative to the effective density of states, and using equations 17 and 20 when this condition is not satisfied.

2.3.2. Field-enhanced carrier capture and emission by tunneling

Large electric fields may greatly increase the rate of carrier capture and emission by traps through band-to-trap tunneling with energy dissipation by phonon excitation [8-11]. In this process, field-induced band-bending lowers the relative energy of band states in the vicinity of a trap, both increasing the carrier population of these states and reducing the energy that must be exchanged with the phonons during the tunneling-enabled capture. Simplifying for computational efficiency, Schenk [10] has replaced the treatment of discrete phonon transitions with a continuum approximation leading to an integral formulation; has approximated the phonon spectrum by one effective phonon mode with energy ħω; has normalized the capture coefficient to its value at zero field, removing poorly known parameters; has assumed that carrier concentrations within tunneling range of a trap vary with location in accord with local thermodynamic equilibrium; and has treated field-enabled tunneling to a trap from the neighboring region as an effective enhancement of the zero-field trapping from band states at the trap. In this formulation, the carrier capture rate per unit volume by traps of type Z is expressed in terms of the carrier concentration at the location of the trap. For conduction electrons the field-enhanced capture rate is given by:

$$U\{Z,e\}(F) = U\{Z,e\}(F=0) + U^{tun}\{Z,e\}(F) = \sigma_0^e v_{th}^e \left(1 + \tilde{g}^e(F)\right) [Z]\, n^e \ . \qquad (21)$$

where $U\{Z,e\}(F=0)$ is the capture rate at zero field and the field-dependent increase due to tunneling $U^{tun}\{Z,e\}(F)$ is proportional to

$$\tilde{g}^{e}(F) = \frac{\displaystyle\int_0^{E_t^e} dE\ M_c(E)\, T_c(E)\, exp\left(-\frac{E}{kT}\right)}{\displaystyle\int_{E_t^e}^{\infty} dE\ M_c(E)\, exp\left(-\frac{E}{kT}\right)\frac{\sqrt{E - E_t^e}}{\pi}} \ . \qquad (22)$$

where E is the energy relative to the trap state. E_t^e is the trap energy, equal to the energy of the defect and one electron in the conduction band minus the energy of the defect with an electron bound to it, where the defect is in its relaxed minimum energy lattice configuration in both cases.

This is the same quantity as ΔE in equations 14 and 15. Note that equation 22 includes tunneling from the trap to the band edge in the direction of decreasing energy.

With approximations discussed in [10], the multi-phonon transition probability $M_c(E)$ can be expressed as:

$$M_C(E) = \frac{1}{\sqrt{2\pi}}\left(\left(\frac{E}{\hbar\omega}\right)^2 + z^2\right)^{-\frac{1}{4}} exp\left\{-S(2f_B+1) + \sqrt{\left(\frac{E}{\hbar\omega}\right)^2 + z^2} + \frac{E}{2kT}\right. \tag{23}$$

$$\left. - \frac{E}{\hbar\omega} ln\left(\frac{E}{z\hbar\omega} + \sqrt{1 + \left(\frac{E}{z\hbar\omega}\right)^2}\right)\right\},$$

where

$$z = 2S\sqrt{f_B(f_B+1)} \tag{24}$$

and

$$f_B = \left(exp\left(\frac{\hbar\omega}{kT}\right) - 1\right)^{-1} \tag{25}$$

is the Bose function. S is the Huang-Rhys factor, equal to the lattice relaxation energy divided by the phonon energy. The tunneling probability $T_c(E)$ is evaluated from

$$T_c(E) = \frac{1}{4\pi}\frac{(\hbar\Theta)^{\frac{3}{2}}}{E_t^e}\, exp\left(-\frac{4}{3}\left(\frac{E_t^e - E}{\hbar\Theta}\right)^{\frac{3}{2}}\right), \tag{26}$$

where

$$\Theta = \left(\frac{e^2F^2}{2\hbar m^*}\right)^{\frac{1}{3}} \tag{27}$$

is the electro-optical frequency. Band symmetries allow the tunneling mass m^* to be treated as a scalar quantity for GaAs.

In damage cascades, strongly field-enhanced recombination rates combined with very high defect concentrations and transport-limited flow of carriers into the cluster can reduce carrier concentrations by orders of magnitude from equilibrium values. This makes the last two of the above simplifications unsuitable for the present application. We have therefore adapted Schenk's integral formulation in two ways: The relevant carrier concentrations are extracted as a function of location from the model simulation over the range of tunneling instead of assuming that the carrier concentrations are in equilibrium; and carrier removal from the bands is appropriately delocalized rather than being taken to occur entirely at the position of the trap. For brevity, the application of detailed balance to determine the rate of carrier emission from the traps is deferred to section 4.3.

The assumption of local equilibrium is embodied in the factor $exp\left(-\frac{E}{kT}\right)$ in the numerator of equation 22. Assuming constant field over the region of tunneling and defining x=0 at the location of the trap, one has in the numerator a correspondence between x and E given by

$$x = -\frac{E_t^e - E}{e\,F} \tag{28}$$

The assumption of local equilibrium implies

$$n^e(0)\,exp\left(-\frac{E}{kT}\right) = n^e(x)\,exp\left(-\frac{E_t^e}{kT}\right). \tag{29}$$

Substituting into the numerator of equation 22 gives a generalized formulation in terms of the spatially varying carrier concentration without the assumption of local equilibrium:

$$U^{tun}\{Z,e\}(F) = \sigma_0^e v_{th}^e\,[Z]\,exp\left(-\frac{E_t^e}{kT}\right)\frac{\int_0^{E_t^e} dE\,M_c(E)\,T_c(E)\,n^e(x)}{\int_{E_t^e}^{\infty} dE\,M_c(E)\,exp\left(-\frac{E}{kT}\right)\frac{\sqrt{E-E_t^e}}{\pi}}. \tag{30}$$

This is the formulation used in the present model for carrier recombination in clustered defects. It should be noted that the above development is one-dimensional, and that as a result equation 30 is an approximation for the spherical geometry of the present problem, with an accuracy that decreases with tunneling distance.

2.3.3. Reactions among defects and dopants

The sink term for defect-defect and defect-dopant reactions of the type X+Y→Z , between species of type X and Y producing a product of type Z is evaluated using:

$$U\{X,Y\} = 4\pi\,R\,D\,[X][Y] \tag{31}$$

The defect reaction rate is proportional to the concentrations [X] and [Y] of the two reactants, the diffusion coefficient D of the mobile defect and an effective reaction radius R. In some cases there is no product defect, for example in the annihilation reaction between an interstitial and vacancy of corresponding type. Defect reactions are configured to conserve total charge. When a product defect is produced, the charge state of the product is the sum of the charge states of the reactants, provided that is a stable configuration of the product defect as determined by DFT. When the reaction would produce a product defect in a charge state that is not stable, the reaction is taken to produce the defect in the nearest stable charge state, plus electrons or holes to

conserve charge. Reactions of the above type are included only if they are exothermic. Examination of reaction enthalpies, based on defect formation energies determined by DFT, shows that most such processes are sufficiently exothermic to be essentially irreversible at room temperature. Therefore inverse dissociation reactions are presently not included in the model (equation 31), although such reactions could be added if needed.

The reaction radius R in equation (31) is evaluated as follows. If either reacting species is neutral, the reaction radius is equal to the lattice constant a_0=0.565 nm for GaAs. When both species are charged with the same sign the reaction is not included, under the assumption that Coulomb repulsion inhibits the reaction. When the two species are charged with opposite sign the reaction radius is the distance at which the energy of the screened electrostatic interaction equals the thermal energy:

$$\frac{|Q_1 Q_2| e^2}{4\,\pi\,\varepsilon\,R} \exp\left(-\frac{R}{\lambda}\right) = kT \tag{32}$$

with Debye screening length $\lambda = \sqrt{\frac{\varepsilon k T}{e^2 n}}$ from mobile charge with concentration n,

and where Q_1 and Q_2 are the charge states of the reactants.

The code uses an analytic approximation for the root of equation (32) to evaluate the reaction radius:

$$R = 0.65\,\lambda \ln\left(1 + \frac{|Q_1 Q_2| R_0}{0.65\,\lambda}\right) \tag{33}$$

where $|Q_1\,Q_2|\,R_0$ is the reaction radius without screening, and $R_0 = e^2/(4\,\pi\,\varepsilon\,k\,T)$ =4.25 nm for GaAs at 300K. Where the defect concentration is high, the reaction radius calculated from equation (33) may be greater than the mean distance between defects, approximated as $R_{def} = N_{def}^{-1/3}$, where N_{def} is the defect concentration. The reaction radius is therefore reduced so that it does not exceed half the distance between defects:

$$R_m = \frac{1}{\frac{1}{R} + \frac{2}{R_{def}}}\,. \tag{34}$$

3. DEFECT SPECIES AND REACTIONS INCLUDED IN THE MODEL

The selection of defect species and reactions included in the model is guided by calculations of defect properties in GaAs using density functional theory [12-17]. Marlowe and molecular dynamics simulations show that the defects produced in the initial collision cascade include primarily interstitials, vacancies and anti-site defects on the Ga and As sublattices, plus divacancies and di anti-site defects [18]. Of these, only the arsenic and gallium interstitials are potentially mobile at room temperature. These may diffuse and react with dopants and other defects to produce secondary reacted species. One such reaction is a kick-out reaction, for example when an arsenic interstitial displaces a carbon p-type dopant from an arsenic lattice site, producing a carbon interstitial. Similarly, a gallium interstitial can displace a silicon n-type dopant from a gallium site producing a silicon interstitial. DFT predicts that carbon and silicon interstitial atoms may also migrate and react to form tertiary products. The model therefore includes as potentially mobile species, arsenic, gallium, carbon and silicon interstitials. All of the other defect species examined by DFT had large energy barriers for migration and are therefore not significantly mobile by thermally activated diffusion at room temperature.

Defects usually have stable atomic configurations in multiple charge states. A stable atomic configuration is one which has an energy minimum for small displacements. In general, atomic configurations are different for different charge states of a defect. In some cases, various stable configurations exist for a given charge state, in which case the model uses the formation energy of the lowest energy configuration. The accuracy of this approximation is being examined. The influence of intermediate configurations on carrier capture and emission might be more accurately approximated through suitably chosen effective energetics. Table 1 lists the formation energies for the lowest energy configuration of the various charge states Q of interstitial defects which are used in the model. Formation energies are used to calculate carrier emission rates, from equation (15), and to determine the relative populations of the various charge states in thermal equilibrium. These values were obtained by DFT simulations using the plane-wave basis code Soccoro [17], and are estimated to have associated uncertainties of about ±0.1 eV.

Defects migrate by a thermally activated process, in which thermal fluctuations in their local atomic configuration lead to a higher energy saddle-point configuration from which the

lattice relaxes into the original minimum-energy defect configuration on an adjacent site. This leads to random-walk diffusion and to drift in electrostatic fields for charged species; these processes can be described in terms of a diffusion coefficient D, which is isotropic in a lattice with cubic symmetry. The diffusion coefficient is evaluated using

$$D = D_0 \exp(-E_m/kT) \ . \tag{35}$$

Values for D are used in evaluating defect reaction rates (equations 31), and the transport of mobile defects by drift and diffusion (equation 9). Values for energy barriers for thermally activated migration E_m for the mobile defects included in the model are listed in table 2. These migration barriers were determined from calculations of formation energies of relaxed lattice configurations as the defect moves from one site to a neighboring equivalent site. Various pathways or intermediate configurations were explored to find the lowest migration energy. These calculations were done using the plane-wave basis code Soccoro [17].

Values for the diffusion prefactor D_0 are not accurately known, but can be estimated within about an order of magnitude from:

$$D_0 = \frac{1}{6} d^2 \, \nu \tag{36}$$

for a cubic lattice, where d is the hop distance between neighboring sites, and ν is the attempt frequency. Using the optical phonon frequency as the attempt frequency, $\nu = 8\text{x}10^{12}$ Hz [19] and the spacing between like atoms for the hop distance $d = \frac{a_0}{\sqrt{2}}$ =0.40nm, eq(36) gives D_0= 0.002 cm^2/s. In view of uncertainties, we use $D_0=10^{-3}$ cm^2/s as a nominal value for the diffusion prefactor. Defects with migration energies below about 0.5 eV (highlighted in pink in table 2) have sufficient mobility to anneal at a significant rate at room temperature. The migration energy is seen to vary significantly with charge state, giving rise to an important dependence of the defect transport rate on the relative charge states populations, and hence to acceleration of defect reaction rate under carrier injection.

DFT also shows that an additional athermal process for defect migration occurs for the arsenic interstitial [17]. This is the Bourgoin-Corbett mechanism [20] in which a change in charge state causes a change in the minimum-energy configuration such that the new configuration is the same as that of the initial charge state at the saddle point along the migration path. The defect can then migrate athermally by alternating capture of electron and holes. This

process occurs during transitions between the +1 and 0 charge states of the arsenic interstitial. The process is implemented in the model as an additive term to the diffusion coefficients of $As_I(+1)$ and $As_I(0)$, using equation (36) with the frequencies ν equal to the carrier capture rate per defect $\nu=\sigma\ v_{th}\ n$, and the hop distance d equal to the lattice constant times a scale factor with nominal value of 1. Here σ, v_{th} , and n are the capture cross section, thermal velocity and concentration for electrons or holes as used in the reaction equations (14-20). Thus, $As_I(+1)$ makes one hop for each electron capture and $As_I(0)$ makes one hop for each hole capture. This increased diffusion increases both transport and reaction rates for these two species.

Another possible mechanism for athermal or recombination-induced migration is the energy-kick process in which the electronic energy released by carrier capture converts to local atomic motion of sufficient magnitude and direction for the defect to cross a migration saddle point and move to a neighboring site [21-23]. This process is presently not implemented in the model because available information is not sufficient, though it could be included in a manner similar to that described above for the Bourgoin-Corbett mechanism.

Mobile interstitials can react with immobile defects and dopants. Charge states and formation energies of the various reacting and product species, and hence the reaction enthalpies, were determined by DFT using the Gaussian basis code SeqQuest [13-15]. Table 3 lists the reactions between mobile interstitial species and the various primary immobile species examined by DFT. These DFT calculations identify the defect reaction network and which reactions are exothermic and hence likely to occur. The choice of which immobile defect species and reactions to include in the simulation is a trade-off between simplicity and fidelity. Since each defect type has multiple charge states, inclusion of all species in table 3 would require another 64 defect species in addition to the 20 species for the four types of mobile interstitials. This would result in a very large number of defect reactions. This level of detail and complexity would be computationally very demanding and also is probably not justified considering the uncertainty in defect properties and other approximations in the model. Instead, we have taken the approach to include the minimum number of defect species necessary to capture the main features, and approximate the effect of the many immobile defect types through a few representative generic defect types. The present implementation of the model thus includes mobile defect reactions with carbon p-type and silicon n-type dopants, and with three generic immobile defect types, each with three charge states (+1, 0, -1). These are annihilating (A), reacting (R) and non-reacting (N)

defect types. Table 3 includes corresponding reactions with generic immobile species. Generic annihilating defects (A) provide for reactions which leave no product, as for example $As_I+V_{As}\rightarrow 0$. Generic reacting defects (R) provide for reactions which consume reactants and leave a product which may participate in further reactions. Non-reacting defects (N) provide for defects which contribute to carrier recombination but whose concentrations do not evolve with time through defect reactions. Formation energies for the generic defects were chosen to give energy levels at one third and two thirds of the energy gap for the -1/0 and 0/+1 levels respectively. These were chosen to approximate the effect of charge states and energy levels determined by DFT for the defect types listed in table 3, which span the full range of the bandgap. Carrier capture and emission reactions are included for all included defect species.

The model thus includes the 33 species listed in table 4 consisting of 2 carriers (electron and holes), 2 dopants (carbon p-type and silicon n-type) , 20 mobile defect species (4 types each with 5 charge states) and 9 generic immobile defect species (three types each with 3 charge states) with 44 charge change reactions and 106 defect reactions. This number of species is similar to the number used in the atomistic model for carrier recombination in silicon developed previously and now in use for QASPR simulations of neutron damage response for Si BJTs [1]. An alternative intermediate level of complexity, which might still be tractable, would be to include the primal immobile defect species (vacancies, divacancy and antisites) while still representing the additional species produced by reactions using generic defect types. This approach could be pursued if the simpler approach is found to be inadequate.

4. METHODS OF SOLUTION

Numerical solution of equations 1 is accomplished through spatial discretization on a radial mesh x_j which may have variable step size. This converts the partial differential equations to a coupled system of ordinary differential equations (ODEs), which are then integrated forward in time from a specified initial condition. The extreme numerical stiffness of the problem and the highly sensitive interdependency of variables require a suitably advanced solver. We employed the ODE solver DDEBDF [24]. An alternative methodology based on a differential-algebraic equation (DAE) solver [25] offers the prospect of greater computational efficiency accompanied by more complexity and stability challenges. Solutions are formulated to produce correct thermodynamic equilibrium and to conserve the number of particles and charge.

Discretization of equation 1 gives:

$$\frac{dn_j^i}{dt} = \frac{(\frac{x_{j-1}+x_j}{2})^2\,\Phi_j^i - (\frac{x_j+x_{j+1}}{2})^2\Phi_{j+1}^i}{x_j^2\left(\frac{x_{j+1}-x_{j-1}}{2}\right)} + (reaction\ terms)_j \tag{37}$$

for the time derivative of concentrations of species i at radial mesh index j>1, where Φ_j^i is the flux from radius x_{j-1} to x_j. Here we use the notation that the superscript denotes the species index and the subscript denotes the radial mesh index. At the origin j=1 and x_1=0 and

$$\frac{dn_1^i}{dt} = -6\frac{\Phi_2^i}{x_2} - (reaction\ terms)_1\ . \tag{38}$$

4.1. Flux equation

Numerical evaluation of the flux is accomplished by a generalization of the approximation originally described by Scharfetter and Gummel [26] for Boltzmann carrier statistics:

$$\Phi_j^i = -\mu^i\,\frac{q^i}{|q^i|}\,\frac{\Delta V_j}{\Delta x_j}\,\frac{n_j^i\exp\left(\frac{q^i\Delta V_j}{2kT}\right) - n_{j-1}^i\exp\left(-\frac{q^i\Delta V_j}{2kT}\right)}{\exp\left(\frac{q^i\Delta V_j}{2kT}\right) - \exp\left(-\frac{q^i\Delta V_j}{2kT}\right)} \tag{39}$$

where

$$\Delta V_j = V_j - V_{j-1}\ , \tag{40}$$

$$\Delta x_j = x_j - x_{j-1}\ ,$$

V_j is the electrostatic potential at the mesh points and q=Qe is the charge (with charge state Q=-1 for electrons, +1 for holes). Equation 39 is exact for steady-state flow under uniform field, yields thermodynamic equilibrium correctly at zero flow, and approaches the correct derivative form as Δx goes to zero. The flux of mobile defects with charge $q \neq 0$ is calculated using equation 39 with an equivalent mobility derived from the diffusivity using equation 6. For neutral defects, the flux is evaluated from

$$\Phi_j^i = -D^i \frac{\Delta n_j^i}{\Delta x_j} \tag{41}$$

Equation 39 is used to evaluate the fluxes of charged defects and of carriers when their concentrations are small compared to their effective density of states. When this condition is not satisfied, Fermi-Dirac statistics must be used. In this case the carrier flux is calculated using a modified form of equation 39:

$$\Phi_j^i = -\mu^i \frac{q^i}{e} \frac{\Delta V_j}{\Delta x_j} \sqrt{n_j^i \, n_{j-1}^i} \; \frac{\exp\left(\frac{q^i\left(\Delta V_j - \frac{\Delta\psi_{cj}}{e}\right)}{2kT}\right) - \exp\left(\frac{-q^i\left(\Delta V_j - \frac{\Delta\psi_{cj}}{e}\right)}{2kT}\right)}{\exp\left(\frac{q^i \Delta V_j}{2kT}\right) - \exp\left(-\frac{q^i \Delta V_j}{2kT}\right)} \tag{42}$$

where Q=-1 for electrons and Q=+1 for holes and

$$\Delta\psi_{cj} = \psi_{cj} - \psi_{cj-1} \tag{43}$$

are evaluated from the carrier concentrations using equation 7. The form of Eq. 42 was chosen to satisfy three criteria: reduction to Eq. 39 when carrier concentrations are small compared to the density of states; correct thermodynamic equilibrium at zero flow; and reduction to the correct derivative form as Δx goes to zero. Equation 42 is used only at the higher concentrations where it is required; Eq. 39 leads to greater stability in the numerical solution at small concentrations, where zero and even negative concentration values can arise temporarily as the calculation proceeds.

4.2. Poisson's equation

Poisson's equation is solved at each time step. The numerical method used is to advance the spatial integration of equation 10 from the center of the sphere to the outer boundary using the exact solution for the case where the charge density varies linearly between mesh points,

$\rho/\varepsilon = \gamma+\beta\rho$, with the boundary condition that the field and potential are zero at the center. This integration uses the same spatial discretization as that used for solving the transport equations. The discretized equations for this case are:

$$V_i = a_i + \frac{b_i}{x_i} - \frac{1}{6}\gamma_i x_i^2 - \frac{1}{12}\beta_i x_i^3 \tag{44}$$

$$F_i = \frac{b_i}{x_i^2} + \frac{1}{3}\gamma_i x_i + \frac{1}{4}\beta_i x_i^2$$

$$\beta_i = \frac{\rho_i - \rho_{i-1}}{\varepsilon(x_i - x_{i-1})}$$

$$\gamma_i = \frac{\rho_{i-1}}{\varepsilon} - \beta_i x_{i-1}$$

$$a_i = V_{i-1} - \frac{b_i}{x_{i-1}} + \frac{1}{6}\gamma x_{i-1}^2 + \frac{1}{12}\beta_i x_{i-1}^3$$

$$b_i = F_{i-1}\, x_{i-1}^2 - \frac{1}{3}\gamma x_{i-1}^3 - \frac{1}{4}\beta_i x_{i-1}^4 \ ,$$

At the center (i=1) x_1, V_1, F_1, a_1, and b_1 all have values of zero.

These equations give the potential V_i and field F_i at the mesh points x_i . Evaluation of the fluxes (equations 39 and 42) uses these potentials at the mesh points, but employs carrier mobilities corresponding to the field midway between mesh points, approximated as

$$F_i = -\frac{V_i - V_{i-1}}{x_i - x_{i-1}} \ . \tag{45}$$

The Poisson solver allows three options for charge compensation:

i no compensation

ii subtract uniform background charge to give zero total charge density at the boundary. This is used for simulations of recombination in a depletion region where charge on ionized dopants would give a spurious radial electric field not present in a device.

iii subtract a uniform background charge to make the total contained charge and the field at the boundary equal to zero.

4.3. Carrier capture and emission reactions

Reaction rates for carrier capture and emission by defects, not involving field-enhanced tunneling, are calculated by direct application of equations 16,17,19 and 20 at the mesh points x_j. Evaluation of field-enhanced capture and emission between spatially separated traps and band states is based on equation 30. The integral in the numerator of equation 30 is discretized by centering its segments on the simulation mesh elements. The back reaction, omitted above for simplicity, is now included. The reaction rate between traps at x_j and electrons at x_k is

$$U_{jk}^{tun}\{Z_Q, e\} = \sigma_0^e \nu_{th}^e R_{jk} \left(n_k^e \, [Z_Q]_j - N_c \, [Z_{Q-1}]_j \, exp\left(-\frac{\Delta E_{Q-1} - e\,V_k + e\,V_j}{k\,T} \right) \right) \tag{46}$$

in the case of Boltzmann statistics and

$$U_{jk}^{tun}\{Z_Q, e\} = \sigma_0^e \, \nu_{th}^e \, R_{jk} \, n_k^e \left([Z_Q]_j - [Z_{Q-1}]_j \, exp\left(-\frac{\Delta E_{Q-1} - eV_k + eV_j - E_k^c + E_k^F}{k\,T} \right) \right) \tag{47}$$

for Fermi-Dirac statistics where

$$R_{jk} = \frac{M_c(\Delta E_Q - eV_k + eV_j)\, T_c(\Delta E_Q - eV_k + eV_j)\, exp\left(-\frac{\Delta E_Q}{kT}\right) \left(\frac{e|V_{k+1} - V_{k-1}|}{2}\right)}{\int_{\Delta E_q}^{\infty} dE\, M_c(E)\, exp\left(-\frac{E}{kT}\right) \frac{\sqrt{E - \Delta E_Q}}{\pi}} \tag{48}$$

with corresponding equations for holes. Particle conservation is achieved by a volume correction for spherical geometry in the equation for the change in carrier concentration. Thus, for defects

$$\left.\frac{d[Z_Q]_j}{dt}\right|^{tun} = -\sum_{k \neq j} U_{jk}^{tun} \{Z_Q, e\} \tag{49}$$

while for carriers

$$\left.\frac{dn_k}{dt}\right|^{tun} = -\sum_{j \neq k} U_{jk}^{tun}\{Z_Q, e\} \left(\frac{x_j}{x_k}\right)^2 \left(\frac{x_{j+1} - x_{j-1}}{x_{k+1} - x_{k-1}}\right) \tag{50}$$

Here, the summation over k is in the direction of decreasing energy E. This formulates the reaction rates in terms of concentrations and electrostatic potentials at the mesh points.

4.4. Evaluation of inverse Fermi integral

The code calculates carrier chemical potentials from their concentrations according to equation 7, using the Joyce-Dixon approximation [27] for the inverse Fermi integral for parabolic bands when x<7.5, and an expression suggested by Blakemore [28]

$$\mathcal{F}_{1/2}^{-1}(x) = \left[\left(\frac{3\sqrt{\pi}}{4}\,x\right)^{\frac{4}{3}} - \frac{\pi^2}{6}\right]^{\frac{1}{2}} \tag{51}$$

when x>8.5, where $x=n^e/N_C$ for electrons and $x=n^h/N_V$ for holes. The gap between 7.5<x<8.5 is bridged using a pair of connected parabolas chosen to maintain a continuous first derivative.

4.5. Boundary conditions

At the outer boundary, a reflecting boundary condition (flux=0) is always used for mobile defects. The code provides three options for the boundary condition on carrier concentrations at the outer boundary:

a) concentration of electrons and holes are set to the equilibrium value

b) no flow of carriers through the boundary, i.e. reflecting boundary and total contained charge is conserved

c) concentrations of electrons and holes are set to constant specified values.

Option b) is imposed as described above for defects. Because we are using an ODE solver, values for the time derivative of concentrations at the boundary must be specified rather than values of concentrations. Thus, boundary conditions a) and c) are implemented by setting the time derivatives at the boundary to:

$$\frac{dn}{dt} = (n_o - n)/\tau \tag{52}$$

where $$\tau = \frac{\Delta x^2}{D}\,.$$

is a time constant for diffusion between mesh points with diffusion coefficient $D = \frac{\mu kT}{e}$. This is a source/sink term for carriers at the boundary which causes the value of the carrier concentration at the boundary to rapidly approach the specified value n_0, without upsetting the ODE integrator.

The boundary conditions on the solution of Poisson's equation are that the electrostatic potential and electric field are both zero at zero radius.

4.6. Initial conditions

The initial condition used in the model is that the concentrations of electrons and holes are equal to the concentrations of n and p-type dopants respectively, the dopants are ionized, and the defects are initially in their neutral charge state. The initial radial distribution of defects used in the model is obtained from a pair correlation function analysis [1] of defect maps calculated by Philip Cooper, using the binary collision code Marlowe [2]. For the simulation discussed here, the Marlowe calculations used a distribution of recoil energies for neutrons with an energy spectrum for the Sandia pulsed reactor SPR III central cavity [29]. The recoil energy distribution was calculated using the Empire nuclear reaction code [30]. The radial concentration profile was obtained from the vacancy-vacancy pair correlation function. This was done by first calculating the pair correlation function from the Marlowe defect maps for a large number of collision events. The pair correlation function was also calculated using an analytic representation of the radial concentration profile. Coefficients in the analytic formula are determined from a multi-parameter least-square minimization of the difference between the pair correlation functions calculated from the defect maps and from the analytic expression. Good agreement is obtained using a polynomial-based expression for the radial defect concentration profile:

$$n(x) = n_0 \exp\left[\sum_{i=1}^{m} a_i \left(ln\left(\frac{x}{x_0}\right)\right)^{i-1}\right] \tag{53}$$

where x is the radius and n_0=1 nm^{-3} and x_0=1 nm, shown in figure 1. An alternative analytic expression for the radial concentration profile which also gives a good fit to the pair correlation function is:

$$n(x) = \frac{1}{4\pi x^2}\frac{N}{\lambda}\exp(-\frac{x}{\lambda}) \tag{54}$$

where N is the number of defects in the cluster and λ is the mean radius.

4.7. Verification

Multiple verification tests of the model were conducted by running simulations designed to test specific functionalities of the code for conditions where analytical solutions are available. The good agreement between the model and the analytic solutions confirmed that the model was

solving the equations as intended. These calculations are described in detail in a separate report [31].

5. SIMULATIONS

The objective of this work is to develop a model for carrier recombination that captures experimentally observed trends and to demonstrate that agreement with experiment can be achieved with modest adjustment of parameters. Here we present results of simulations and compare to experimental information, specifically, to measurements of transient gain in HBTs. In HBTs, increased carrier recombination at damage increases the base current and decreases the gain. Thus, measurements of HBT gain change after pulsed neutron and ion irradiation provide data which can be used for calibration and validation of the recombination model. The goal here is to establish suitability of the approach, with more complete calibration and validation to follow. Simulations discussed in this section do not include field-enhanced carrier recombination due to tunneling, which is discussed in the following section.

For the simulation discussed here, the material is GaAs carbon doped at a concentration of $5x10^{19}/cm^3$, corresponding to the base of an Npn HBT. The defect radial concentration profiles described in section 4.6 were used. The vacancy concentration was limited at a maximum value of 1 atomic percent in the cluster core to represent rapid spontaneous recombination of defects when their separation approaches a lattice constant. The concentration of annihilating defects was taken to be the vacancy concentration and the concentration of arsenic and gallium interstitials were each taken to be half the vacancy concentration. This approach provides representative initial radial defect concentration profiles which are plotted in figure 2. The open circles show the initial concentrations for arsenic interstitials and annihilating defects. Gallium interstitials (not shown) have the same initial concentration profile as arsenic interstitials. Figure 2 also shows the concentrations of electrons and holes, which depart significantly from their boundary values at radii less than about 20 nm. The maximum radius, i.e. radius of the outer boundary of the simulation was chosen to be 100 nm. At this value, the defect concentrations and electric field are very small, and the carrier flow into the cluster is insensitive to the boundary radius value.

Defect parameter values used in the simulations are listed in Table 4. Formation and migration energies were obtained from DFT as discussed in section 3. Capture cross sections

must be treated as adjustable parameters to be determined by comparing simulations with experimental information. As a point of departure, physically reasonable values for capture cross sections were initially chosen which depend on the electrostatic interaction, 10^{-17} cm^2 for repulsion, 10^{-16} cm^2 when either defect is neutral, and 10^{-15} cm^2 for attraction. Values of cross sections are then adjusted from these nominal values to obtain agreement with experimental information. In particular, capture cross sections were increased for carbon interstitials and decreased for gallium interstitials. This adjustment increases the relative influence of the carbon interstitials on carrier recombination. These cross sections give qualitative agreement between time dependence of net carrier recombination in the simulation, and experimentally observed time dependence of gain recovery of Npn HBTs after pulsed damage as shown in figures 3 and 4. Figure 3 shows the carrier flow into the cluster versus time from simulations with the defect parameters in table 4. This simulation used carrier concentration at the outer boundary fixed at values $5x10^{19}/cm^3$ for holes, equal to the carbon dopant concentration, and $10^{15}/cm^3$ for conduction electrons, corresponding to the minority carrier concentration in the neutral region of the base of the Npn HBT (determined by TCAD modeling) at bias conditions used in the measurement of the data in figure 4. In the simulation discussed here, the concentrations of reacting and nonreacting defects were set to zero.

Figure 4 shows measurements of annealing factor versus time for InGaP/GaAs/GaAs (emitter/base/collector) Npn HBTs after pulsed ion irradiation with 3 MeV silicon ions in tests with emitter current fixed at 0.9 milliamp, and ion fluences of $2x10^8$ and $8x10^8$ ions/cm^2, and pulse duration from 20 to 60 microsecond. The ion energy was chosen to place the damage peak at the depth of the device. The annealing factor is the inverse gain change due to the damage, normalized to the value at one second after the pulse. The time dependence of the annealing factor is insensitive to the amount of damage, and has been shown to be similar for damage from neutrons and end-of-range ions [32]. A striking feature of this data is the extended time scale of the gain recovery, which follows a nearly logarithmic time dependence over seven decades in time. This feature of the data is reproduced by the model, as shown in figure 3, with appropriate choice of carrier capture cross sections.

This approach to model calibration assumes that the gain degradation in the HBT is mainly due to carrier recombination in the neutral region of the p-type base of the device. However, carrier recombination in the emitter-base depletion region might also contribute to

HBT gain degradation. Although the wider bandgap of the InGaP emitter material greatly reduces the minority carrier concentration and hence carrier recombination in the depletion region, a large electric field might enhance the carrier capture rate in this region as discussed in section 2.3.2. The influence of the depletion region on HBT gain recovery is presently under further investigation, both by device simulations and by experimental studies of carrier capture and emission in low-field environments in irradiated material. Properties of GaAs used in the model apart from radiation effects are widely documented [19, 33-36] and are not presented in detail here.

The primary output from the simulation is the carrier recombination rate versus time which is given by the flow of conduction electrons into the cluster shown in figure 3. Noteworthy features are an increase at short times ($t<10^{-6}$ sec) and an extended decrease at longer times ($t>10^{-4}$ seconds) which is approximately proportional to log(t) over a broad range of time. For comparison, figure 3 also shows the recombination for the same number of defects uniformly distributed, i.e. without clustering (blue open circles). Clustering increases the magnitude of the recombination and the rate of decrease with time.

The cause of the change in recombination with time in the model can be inferred from the evolving defect concentration profiles. The initial increase in carrier recombination at short times is due to the reaction of arsenic interstitials, mainly with carbon dopants to produce carbon interstitials by the kick-out reaction. The decrease at longer times is due to reaction of carbon interstitials, which occurs more rapidly at smaller radii. The solid lines in figure 2 show the concentrations of defects vs radius after 1 second, by which time the arsenic interstitials have all reacted and carbon interstitials have mostly reacted at small radii $r<10$ nm, but are still present at $r>10$ nm. Figure 5 shows the concentration profiles of the various charge states of the carbon interstitial at t=1 second with a minority electron concentration at the boundary of $10^{15}/cm^3$ (dashed lines) and the corresponding profiles with no excess minority carriers at the boundary (solid lines), corresponding to cases with and without current in a device. Without excess electrons, the carbon interstitials are mainly in the 2+ charge state, which has a high activation energy for diffusion and hence low mobility and slow reaction rate at room temperature. However, increasing the minority electron concentration at the boundary increases the population of the more mobile neutral charge state of the carbon interstitial. Increased electron concentration thus increases the mobility of the carbon interstitial and increases the reaction rate and the rate at

which carrier recombination decreases with time. Figure 6 illustrates that the simulations show faster recovery of carrier recombination at higher minority carrier concentrations. This is qualitatively consistent with the experimental observation that gain recovery in irradiated HBTs occurs more rapidly at higher operating current, also referred to as current-induced, recombination-induced or carrier injection annealing.

Figure 7 shows the flow of electrons versus radius at various times. Most of the recombination occurs at radii less than 20 nm and the changes in recombination in this time range occur at radii between 7 and 15 nm. Figure 8 shows the electric field produced by the charge on the defects. The field exceeds $2x10^5$ V/cm in the region where significant carrier recombination is occurring. In the next section we examine whether these fields might significantly increase the carrier recombination rate.

6. EFFECT OF FIELD-ENHANCED BAND TO TRAP TUNNELING ON CARRIER RECOMBINATION

Calculation of the field-enhanced carrier recombination as described in section 2.3.2 involves evaluation of Mc and Tc in equation 22, and 48 and thus requires values for the effective phonon energy $\hbar\omega$, and the lattice relaxation energy E_R or Huang-Rhys factor $S= E_R/\hbar\omega$. Values for these parameters have been determined from deep-level transient spectroscopy (DLTS) experiments on GaAs diodes irradiated with 3 MeV electrons [37]. The DLTS experiments measured the rate of electron emission vs field strength and temperature for various types of traps with differing binding energies. In general, the data showed faster emission at higher fields in good agreement with the phonon-assisted field-enhanced band-to-trap tunneling model used here. By detailed balance, the enhancement in the carrier capture rate as used in equations 20,46 and 47 is equal to the enhancement in the emission rate. For the deepest trap, the best fit between the tunneling model and the DLTS data gave parameter values of S=15.7, $\hbar\omega$=0.015 eV, Et=0.66 eV for the trap energy. The fit also gave a value of $3.5x10^{-7}$ cm^3s^{-1} for the rate coefficient for electron capture at zero field at T=300K, corresponding to a capture cross section of $0.9x10^{-14}$ cm^2. Values for the carrier mass used in the tunneling model are taken to be the effective mass m*=0.067 me for conduction electrons, while for holes the effective mass of the light-hole valence band m*=0.083 me is used. Figure 9 shows the carrier

capture enhancement factor vs field strength predicted by the model using the above parameter values, and shows that the enhancement reached nearly three orders of magnitude at the maximum field of 0.25×10^6 V/cm sampled in the DLTS experiments. Comparison between figures 8 and 9 shows that charging of defect clusters in heavily doped material produces electric fields high enough to produce large enhancement of carrier recombination. This implies that influence of field-enhanced capture on overall carrier recombination should be explored. Moreover, fields in the depletion region of the emitter-base junction of the Npn HBT are also high enough to produce large enhancement of carrier capture, which indicates that this process may also need to be included in the device models.

Figures 10 and 11 show results from simulations using the cluster model with static clustered defects with and without field-enhanced recombination. A single defect type was used with three charge states with formation energies chosen to give energy levels at 1/3 and 2/3 of the bandgap. Figure 11 shows that with tunneling, carriers recombine at greater radii. However, the increase in total recombination, or flow into the cluster, is small because in this example recombination is limited mainly by carrier transport rather than by the carrier capture cross section. The field-enhanced carrier capture cross sections in the high-field core region, together with the transport-limited flow causes the carrier concentrations in this region to decrease by a large factor as shown in figure 11. This example shows that tunneling can strongly affect carrier recombination, but also that other processes, such as carrier transport, can reduce the net effect of this enhancement on overall carrier recombination.

7. CONCLUSION

The objective of this work was to develop a model to calculate carrier recombination in clustered damage produced by atomic collisions in GaAs, thereby providing a basis for predicting the transient response of HBTs to pulsed neutron damage. Prediction of device response requires two components, first a model for macroscopic carrier transport which provides local carrier concentrations within the device and second a model for carrier recombination at clustered defects which is the subject of this paper.

The carrier recombination model is based on an atomistic description of carrier capture and emission at the defects and the time evolution resulting from the migration and reaction of

the defects. The model uses a continuum description of diffusion, field drift and reaction of carriers and defects within the cluster. This report describes the physics and equations on which the model is based, and provides details of the numerical methods used for their solution. Properties of the defects are discussed and values for their parameters are given, many of which were obtained from DFT simulations. An important feature which emerges from the simulations is that in neutral doped material the defects become charged. Localization of this charge produces large electric fields, which strongly affect the concentrations of carriers and the various defect charge states within the cluster. This in turn affects the rates of carrier recombination and defect reactions. Another consequence of the electric field is that carrier recombination at defects may be greatly enhanced through band-to-bound state tunneling. A treatment of field-enhanced carrier capture, based on a phonon-enhanced tunneling process, was implemented in the cluster model. Simulations of carrier recombination in defect clusters show that the effect of large field enhancement on carrier recombination may be moderated by other rate-limiting processes, such as carrier transport into the cluster.

Comparison between the recombination model and measurements of transient recovery of the gain of Npn HBTs after pulsed ion-irradiation shows good agreement. The model reproduces several features of the data, including the recovery of device gain by about a factor of two extended over many decades in time, and faster recovery at higher levels of carrier injection.

In summary, major progress towards the objective has been achieved. A model for carrier recombination in clustered damage was developed which captures experimentally observed behavior but knowledge of the physics is not sufficient to enable quantitative predictions without calibration to experiments.

REFERENCES

1. S.M. Myers, P.J. Cooper and W.R. Wampler, Model of defect reactions and the influence of clustering in pulse-neutron-irradiated Si, J. Appl. Phys. **104** (2008) 044507 .doi:10.1063/1.2963697
2. M.T. Robinson and I.M. Torrens, Computer simulation of atomic-displacement cascades in solids in the binary-collision approximation, Phys. Rev. B **9** (1974) 5008. doi:10.1103/PhysRevB.9.5008
3. S.M. Foiles, Detailed characterization of defect production in molecular dynamics simulations of cascades in Si, Nucl. Inst. Methods B **255** (2007) 101. doi:10.1016/j.nimb.2006.11.013
4. J. E. Moussa, S. M. Foiles, and P. A. Schultz, Simulation and modeling of the electronic structure of GaAs damage clusters, , J. Appl. Phys **113** (1013) 093706. doi:10.1063/1.4794164
5. E. Holmstrom, K. Nordlund and M. Hakala, Amorphous defect clusters of pure Si and type inversion in Si detectors, Phys. Rev. B **82** (2010) 104111.
6. D. M. Caughey and R. E. Thomas, Proceedings of the IEEE **55** (1967) 2192.
7. J. J. Barnes, R. J. Lomax and G. I. Haddad, IEEE Transactions on Electron Devices **ED-23** (1976) 1042.
8. C.H. Henry and D.V. Lang, Nonradiative capture and recombination by multiphonon emission in GaAs and GaP, Phys. Rev. B **15** (1977) 989.
9. A. Schenk, An Improved approach to the Shockley-Read-Hall recombination in inhomogeneous fields of space-charge regions, J. Appl. Phys. 71 (1992) 3339.
10. A. Schenk, A model for the field and temperature dependence of Shockley-Read-Hall lifetimes in silicon, Solid-State Electronics **35** (1992) 1585.
11. S. Makrak-Ebeid and M. Lannoo, Quantum model for phonon-assisted tunnel ionization of deep levels in a semiconductor, Phys. Rev. B **25** (1982) 6406.
12. P. A Schultz and O. A. von Lilienfeld, Simple intrinsic defects in gallium arsenide, Modeling and simulation in Materials Science and Engineering **17** (2009) 084007 . doi:10.1088/0965-0393/17/8/084007
13. P. A. Schultz, Simple intrinsic defects in GaAs: Numerical supplement, SAND2012-2675
14. P.A. Schultz, Defect reaction network in C-doped GaAs: Numerical predictions, SAND2012-6659.
15. P.A. Schultz, Defect reaction network in Si-doped GaAs: Numerical predictions, SAND2012-6748.
16. P. A. Schultz, A. F. Wright, and W.R. Wampler, Density Functional Theory Assessment of Defects in Neutron-Irradiated III-V Materials, SAND2012-7497P, ASC P&EM FY12 Level 2 milestone report.
17. A. F. Wright, private communication.

18. S.M. Foiles, Comparison of Binary Collision Approximation and Molecular Dynamics for Displacement Cascades in GaAs, Sandia Report SAND2011-8082 2011.

19. Properties of Group IV, IIII-V and II-VI Semiconductors, S. Adachi, Wiley 2005.

20. J.C. Bourgoin and J.W. Corbett, A new Mechanism for Interstitial Migration, Physics Letters **38A** (1972) 135.

21. D. V. Lang and L. C. Kimerling, Observation of recombination-enhanced defect reactions in semiconductors, Phys. Rev. Lett. **33** (1974) 489.

22. J. D. Weeks, J. C. Tully and L. C. Kimerling, Theory of recombination-enhanced defect reactions in semiconductors, Phys. Rev. B **12** (1975) 3286.

23. L. C. Kimmerling, Recombination enhanced defect reactions, Solid-State Electronics **21** (1978) 1391.

24. L. F. Shampine and H. A. Watts, DEPAC – Design of a User-Oriented Package of ODE Solvers, Sandia Report SAND79-2374. http://www.netlib.org/slatec/src/ddebdf.f

25. K.E. Brenan, S.L. Campbell and L.R. Petzold, Numerical Solution of initial-value problems in differential-algebraic equations, Society for Industrial and Applied Mathematics 1996. http://www.cs.ucsb.edu/~cse/index2.php?software.html

26. D. L. Scharfetter and H.K. Gummel, Large-Signal Analysis of a Silicon Read Diode Oscillator, IEEE Transactions on Electronic Devices **ED-16** (1969) 64.

27. W. B. Joyce and R.W. Dixon, Analytic approximations for the Fermi energy of an ideal Fermi gas, Appl. Phys Lett. **31** (1977) 354.

28. J.S. Blakemore, Approximations for Fermi-Dirac integrals, Solid State Electronics **25** (1982) 1067.

29. P.J. Griffin, J.G. Kelly and D.W. Vehar, Updated neutron spectrum characterization for SNL baseline reactor environments, Sandia report SAND93-2554 1994

30. M. Herman, R. Capote, B.V. Carlson P. Obložinský A. Trkov M. Sin H. Wienke V. Zerkin, EMPIRE: Nuclear Reaction Model Code System for Data Evaluation, Nuclear Data Sheets 108 (2007) 2655. http://dx.doi.org/10.1016/j.nds.2007.11.003 http://www.nndc.bnl.gov/empire/

31. Verification testing of Cluster Code for GaAs, W.R. Wampler 11/21/2013, Sandia internal report.

32. D. B. King et al, Experimental Comparison of neutron and Ion Damage in an Npn III-V HBT, Journal of Radiation Effects vol **31**, no 1 pages 141- 150, July 2013.

33. Properties of Gallium Arsenide, Third Edition Edited by M.R. Brozel and G.E. Stillman, EMIS Data Review Series No. 16, INSPEC The Institution of Electrical Engineers, London, UK 1996.

34. Properties of Group-IV, III-V and II-VI Semiconductors, Sadao Adachi, Wiley 2005.

35. J.S. Blakemore, Semiconducting and other major properties of gallium arsenide, J. Appl. Phys. **53** (1982) R123.

36. I. Vurgaftman et. al., Band parameters for III-V compound semiconductors and their alloys, J. Appl. Phys. **89** (2001) 5815.

37. R. M. Fleming, manuscript in preparation.

TABLES

8. Q	As_I	Ga_I	C_I	Si_I
3	2.33	2.03		
2	3.00	2.09	3.93	1.84
1	2.46	2.09	4.25	3.09
0	3.43	4.05	4.89	3.81
-1	4.32	5.17	5.93	5.39
-2			7.22	6.87

Table 1. Formation energies (eV) for various charge states Q of interstitial defects with Fermi energy at the valence band edge. Values were calculated from DFT with plane-wave basis by A. Wright [17].

Q	As_I	Ga_I	C_I	Si_I
3	0.73	1.3		
2	0.17	1.26	0.9	1.2
1	0.45	1.06	0.7	0.75
0	0.38	0.4	0.4	0.6
-1	0.72	0.6	1.2	0.7
-2			0.8	0.9

Table 2 Energy barriers E_m (eV) for thermally activated migration of interstitial defects. Defects with migration energies below about 0.5 eV, highlighted in pink, are mobile at room temperature. Values are calculated from DFT with plane-wave basis by A. Wright [17].

Mobile reactant	Immobile reactant	Reaction product	Generic reactant	Generic product
As_I	C_{As}	C_I	C_{As}	C_I
As_I	Si_{Ga}	$(SiAs)_{Ga}$	Si_{Ga}	R
As_I	V_{As}	0	A	0
As_I	V_{Ga}	As_{Ga}	R	R
As_I	As_{Ga}	$(2As)_{Ga}$	R	R
As_I	Ga_{As}	Ga_I	R	R
As_I	$V_{As}V_{Ga}$	V_{Ga}	R	R
Ga_I	C_{As}	$(CGa)_{As}$	C_{As}	R
Ga_I	Si_{Ga}	Si_I	Si_{Ga}	Si_I
Ga_I	V_{As}	Ga_{As}	R	R
Ga_I	V_{Ga}	0	A	0
Ga_I	As_{Ga}	As_I	R	R
Ga_I	Ga_{As}	$(2Ga)_{As}$	R	R
Ga_I	$V_{As}V_{Ga}$	V_{As}	R	R
C_I	C_{As}	$(2C)_{As}$	C_{As}	R
C_I	Si_{Ga}	-	-	-
C_I	V_{As}	C_{As}	A	C_{As}
C_I	V_{Ga}	C_{Ga}	R	R
C_I	As_{Ga}	$(CAs)_{Ga}$	R	R
C_I	Ga_{As}	$(CGa)_{As}$	R	R
C_I	$V_{As}V_{Ga}$	$C\ V_{As}V_{Ga}$	R	R
Si_I	C_{As}	-	-	-
Si_I	Si_{Ga}	$(2Si)_{Ga}$	Si_{Ga}	R
Si_I	V_{As}	Si_{As}	R	R
Si_I	V_{Ga}	Si_{Ga}	A	Si_{Ga}
Si_I	As_{Ga}	$(SiAs)_{Ga}$	R	R
Si_I	Ga_{As}	$(SiGa)_{As}$	R	R
Si_I	$V_{As}V_{Ga}$	$Si\ V_{As}V_{Ga}$	R	R

Table 3 Expected reactions between mobile defects (first column) and immobile dopants and primal defects (second column) with reaction products (third column) as determined by DFT with Gaussian basis by P. Schultz [13-15]. The subscript denotes the site in the lattice (As, Ga or Interstitial) occupied by the defect. As_{Ga} and Ga_{As} are the two types of anti-site defects. V denotes a vacancy. $V_{As}V_{Ga}$ is a divacancy pair. C_{As} is a p-type dopant and Si_{Ga} is an n-type dopant. Reactions between C and Si are excluded because the material will be either C or Si doped but not both. Fourth and fifth columns indicate corresponding reactions with generic immobile reactants and products of type A (annihilating) representing vacancies or R (reacting) representing other defect types.

Index	Defect	Charge state	Formation Energy (eV)	Migration Energy (eV)	e capture cross section (cm^2)	h capture cross section (cm^2)
1	e	-1				
2	h	+1				
3	C p-dopant	-1	2.95			
4	Si n-dopant	+1	-0.59			
5	As_I	+3	2.33	0.73	1.0e-15	
6	As_I	+2	3.00	0.17	1.0e-15	1.0E-17
7	As_I	+1	2.46	0.45	1.0e-15	1.0E-17
8	As_I	0	3.43	0.38	1.0e-16	1.0E-16
9	As_I	-1	4.32	0.72		1.0E-15
10	Ga_I	+3	2.03	1.30	3.0e-16	
11	Ga_I	+2	2.09	1.26	3.0e-16	3.0e-18
12	Ga_I	+1	2.09	1.06	3.0e-16	3.0e-18
13	Ga_I	0	4.05	0.40	3.0e-17	3.0e-17
14	Ga_I	-1	5.17	0.60		3.0e-16
15	C_I	+2	3.93	0.90	1.0e-14	
16	C_I	+1	4.25	0.70	1.0e-14	1.0e-16
17	C_I	0	4.89	0.40	1.0e-15	1.0e-15
18	C_I	-1	5.93	1.20	1.0e-16	1.0e-14
19	C_I	-2	7.22	0.8		1.0e-14
20	Si_I	+2	1.84	1.20	1.0e-15	
21	Si_I	+1	3.09	0.75	1.0e-15	1.0E-17
22	Si_I	0	3.81	0.60	1.0e-16	1.0E-16
23	Si_I	-1	5.39	0.70	1.0e-17	1.0E-15
24	Si_I	-2	6.87	0.90		1.0E-15
25	A	+1	0		3.0E-16	
26	A	0	0.474		3.0E-17	3.0E-17
27	A	-1	1.422			3.0E-16
28	R	+1	0		3.0E-16	
29	R	0	0.474		3.0E-17	3.0E-17
30	R	-1	1.422			3.0E-16
31	N	+1	0		3.0E-16	
32	N	0	0.474		3.0E-17	3.0E-17
33	N	-1	1.422			3.0E-16

Table 4 Species included in the model with type, charge, and energies of formation and migration for mobile defect species, and carrier capture cross sections.

FIGURES

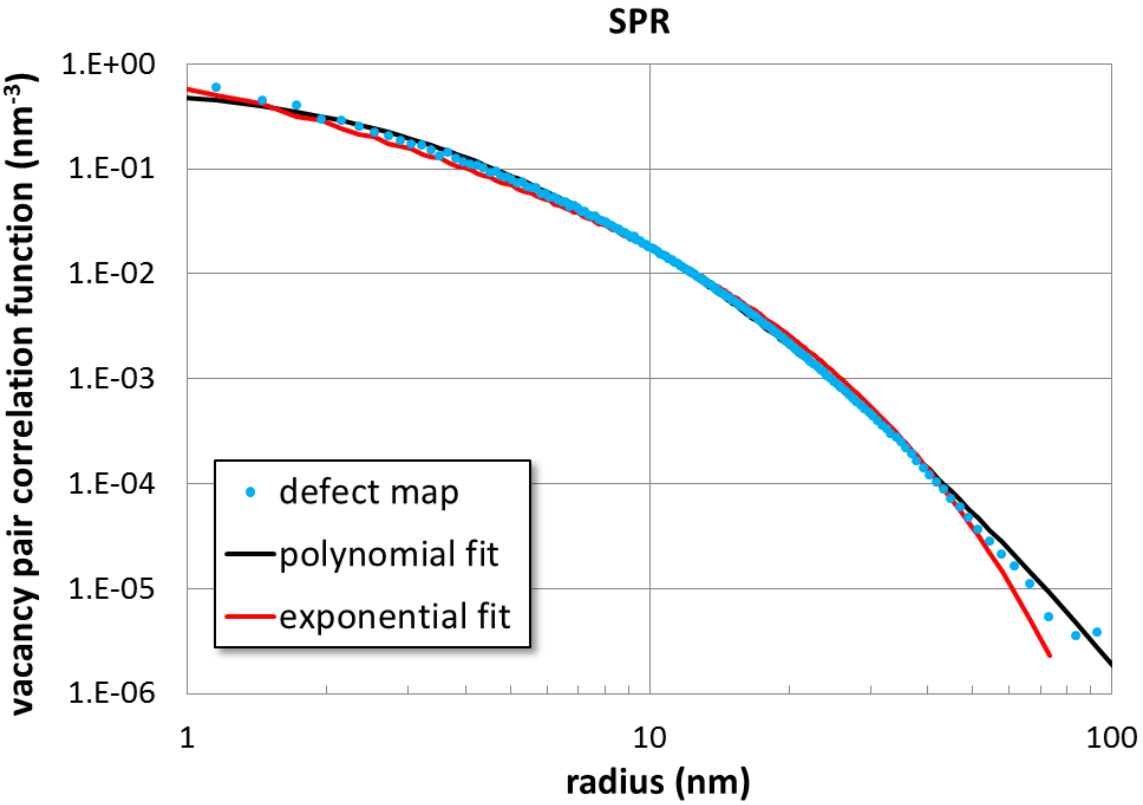

Figure 1 Vacancy pair correlation function calculated from defect maps (symbols) and from analytic expressions for the radial concentration profiles; equation 53 with coefficient values of a_1=1.35, a_2=-1.55 and a_3=-0.384 (black line), and equation 54 with N=530 and λ=10.6 nm (red line).

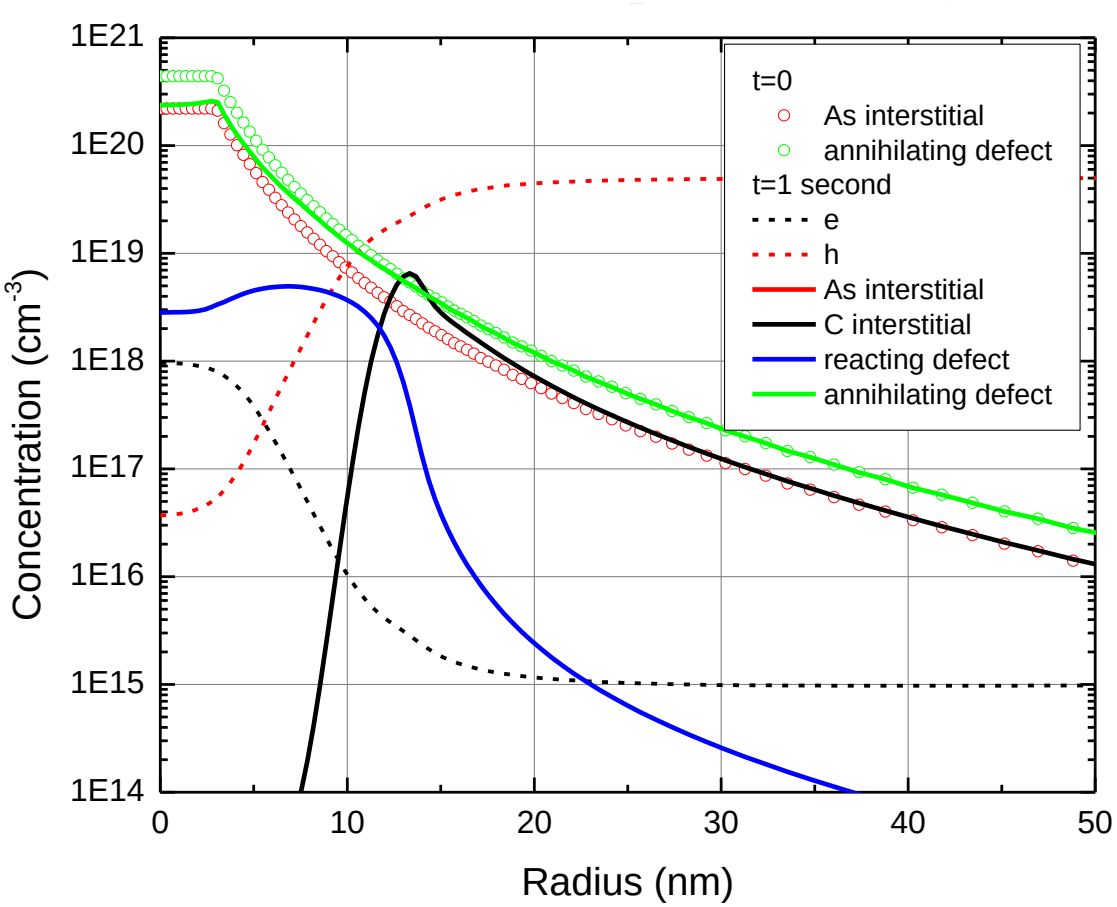

Figure 2. Concentrations vs radius of defects initially (open circles) and after 1 second (solid lines) and of electrons and holes (dashed lines) at 1 second.

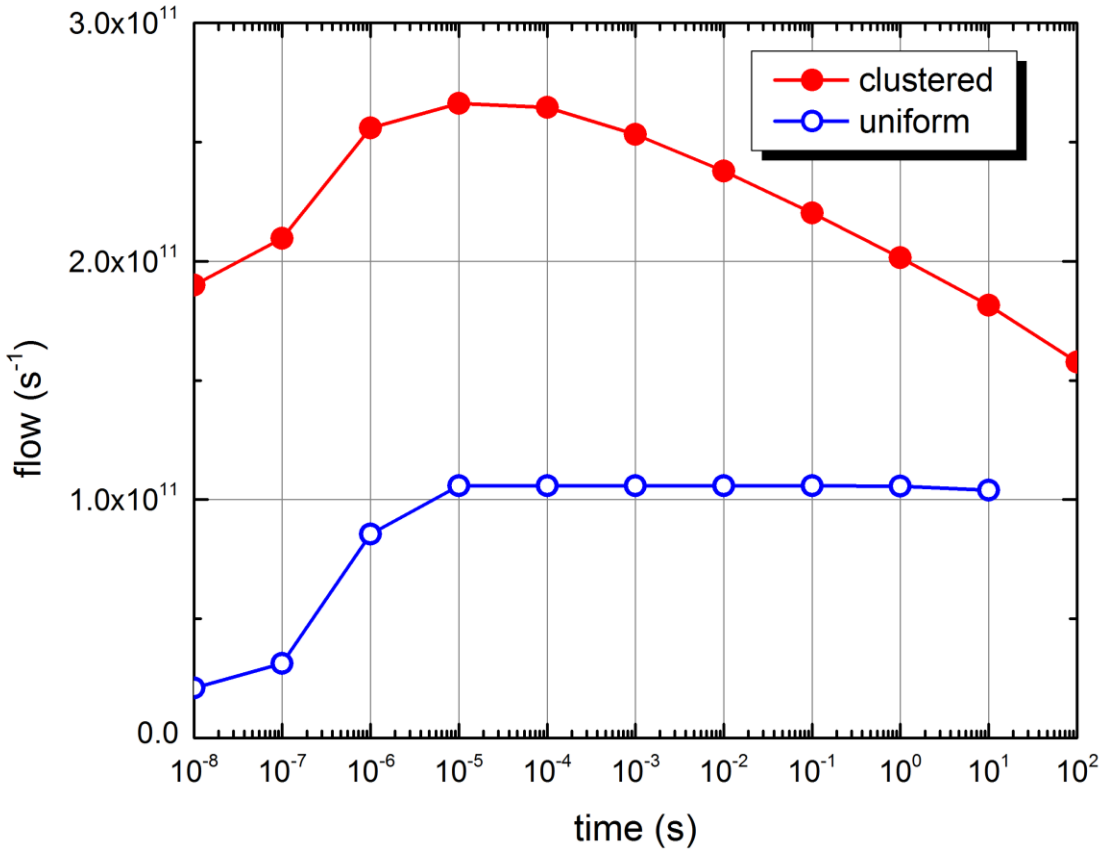

Figure 3 Carrier flow into the cluster, i.e. recombination, vs time after the collision event for clustered damage (red curve with solid symbols), with electron concentration of $10^{15}/cm^3$ at the boundary. To illustrate the influence of defect clustering on carrier recombination, the blue curve with open symbols shows the carrier flow for the same number of defects distributed uniformly.

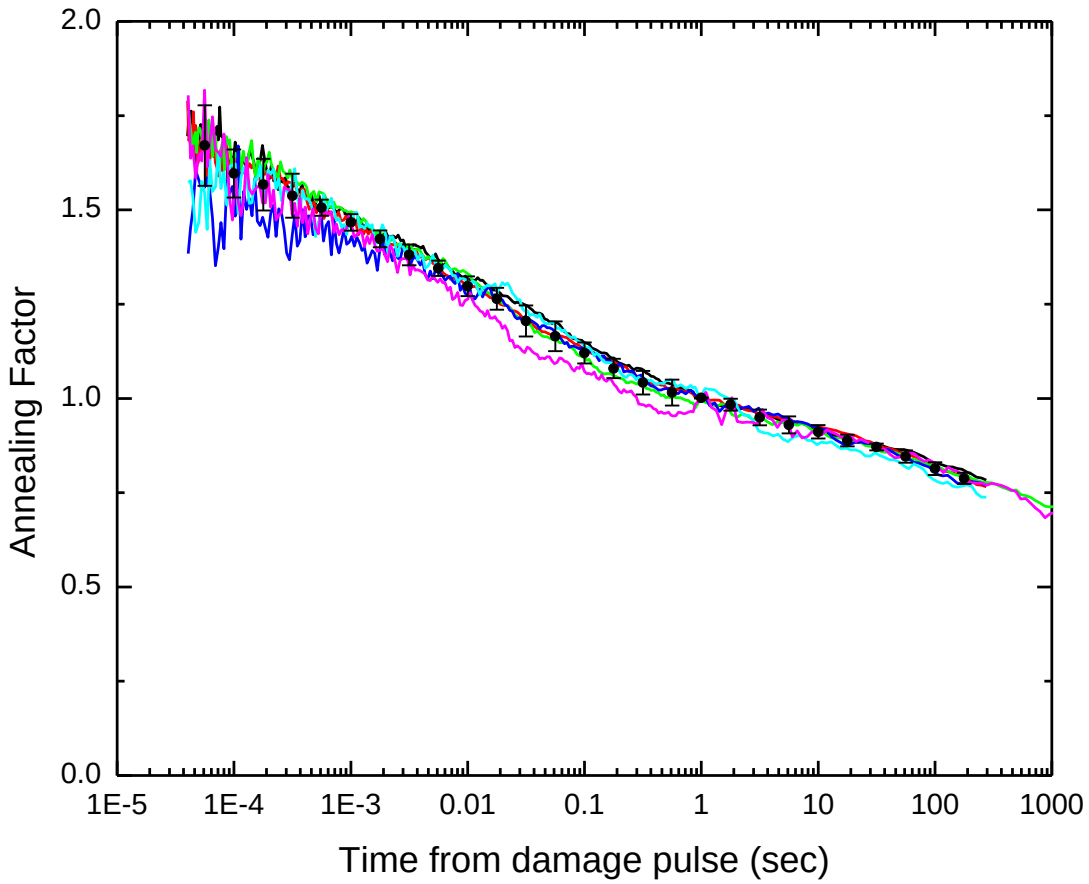

Figure 4. Experimental measurements of the annealing factor versus time after damage from pulsed ion irradiation in InGaP/GaAs/GaAs Npn HBTs, with a device current of 0.9 ma. The annealing factor is the damage-induced change in inverse gain, normalized to the value at one second after the damage pulse. Black symbols with error bars indicate mean values and standard deviation for the six devices shown. (Data provided by D. King, E. Bielejec and G. Vizkelethy)

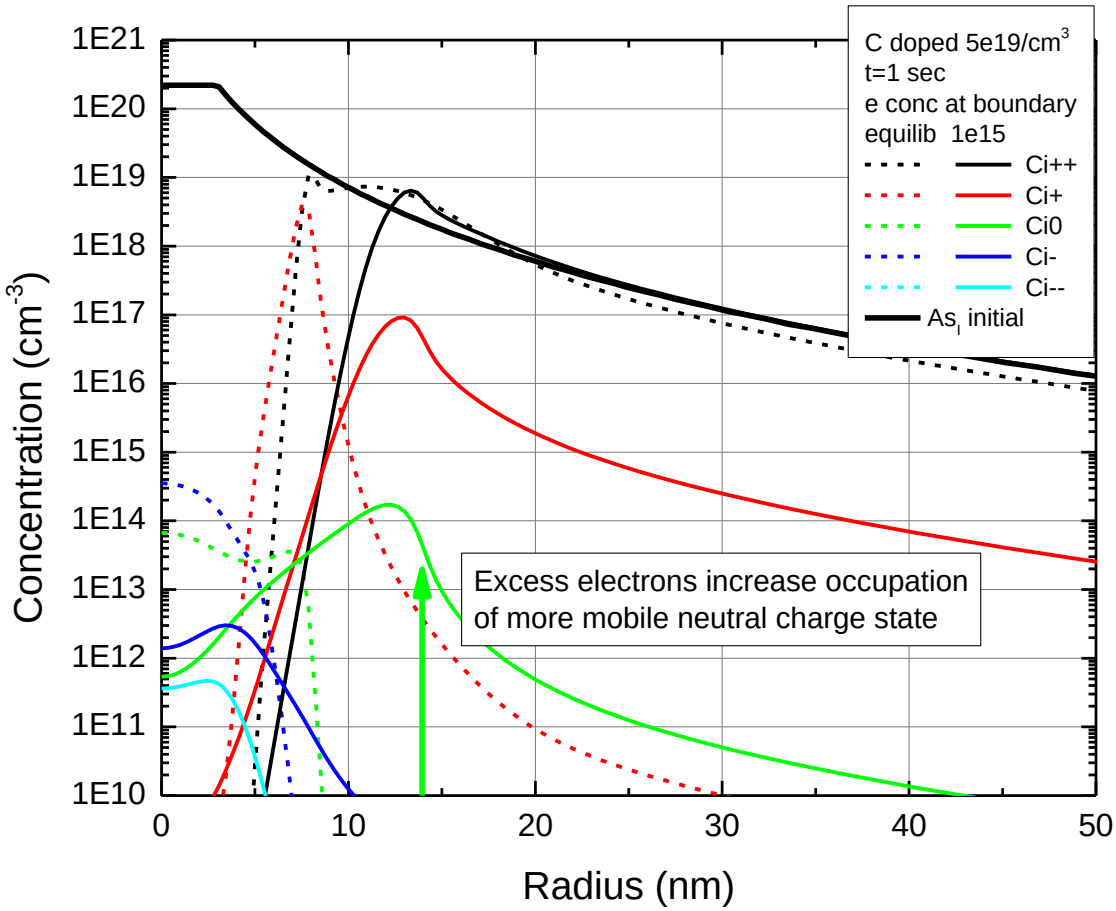

Figure 5. Solid lines show the concentration profiles of the various charge states of the carbon interstitial at t=1 second with a minority electron concentration at the boundary of 1e15/cm^3, and the dashed lines show the corresponding profiles with no excess minority carriers at the boundary. The heavy black line shows the initial concentration of the arsenic interstitial which reacts with carbon dopants to produce the carbon interstitial.

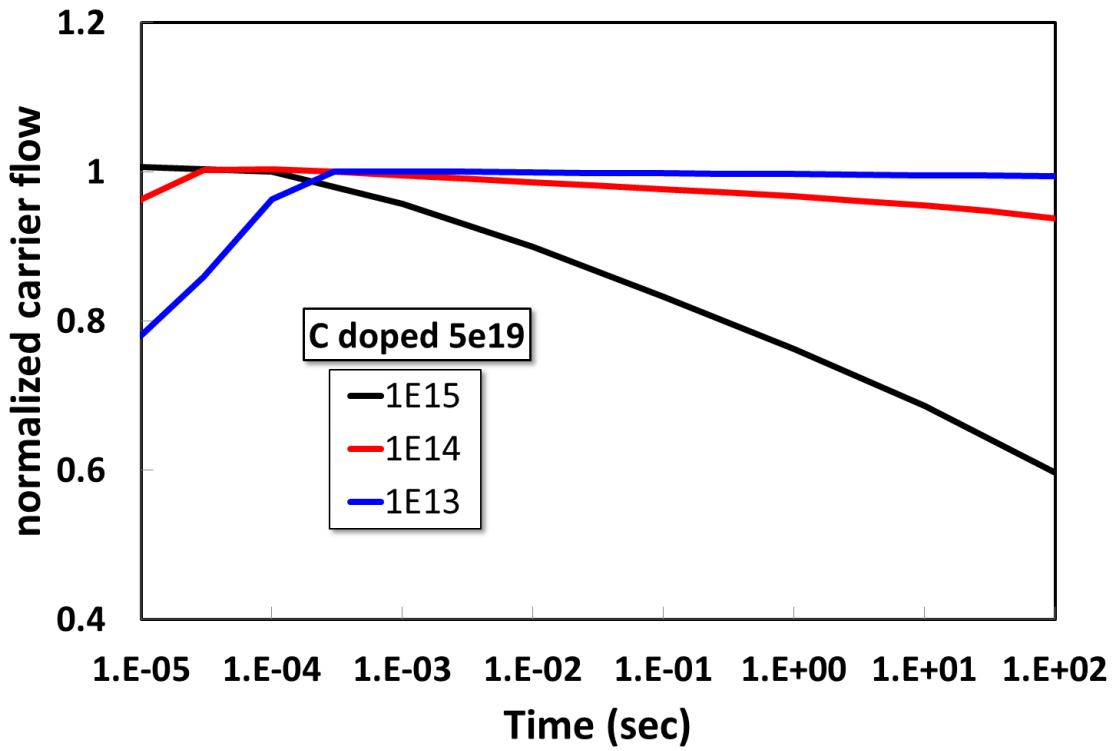

Figure 6. Carrier flow into the cluster, normalized to the peak value, for various values of minority carrier concentration at the boundary indicated in the legend.

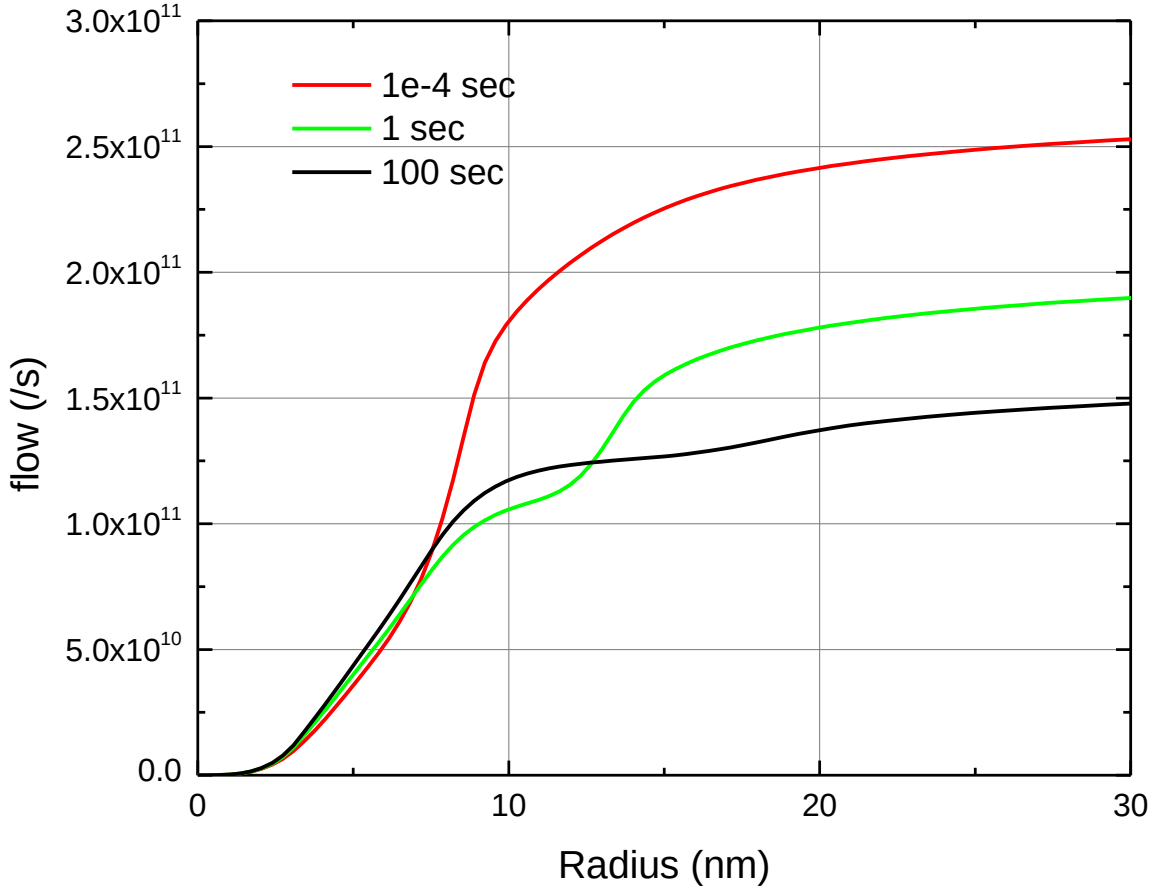

Figure 7. Flow of electrons vs radius at various times indicated in the legend.

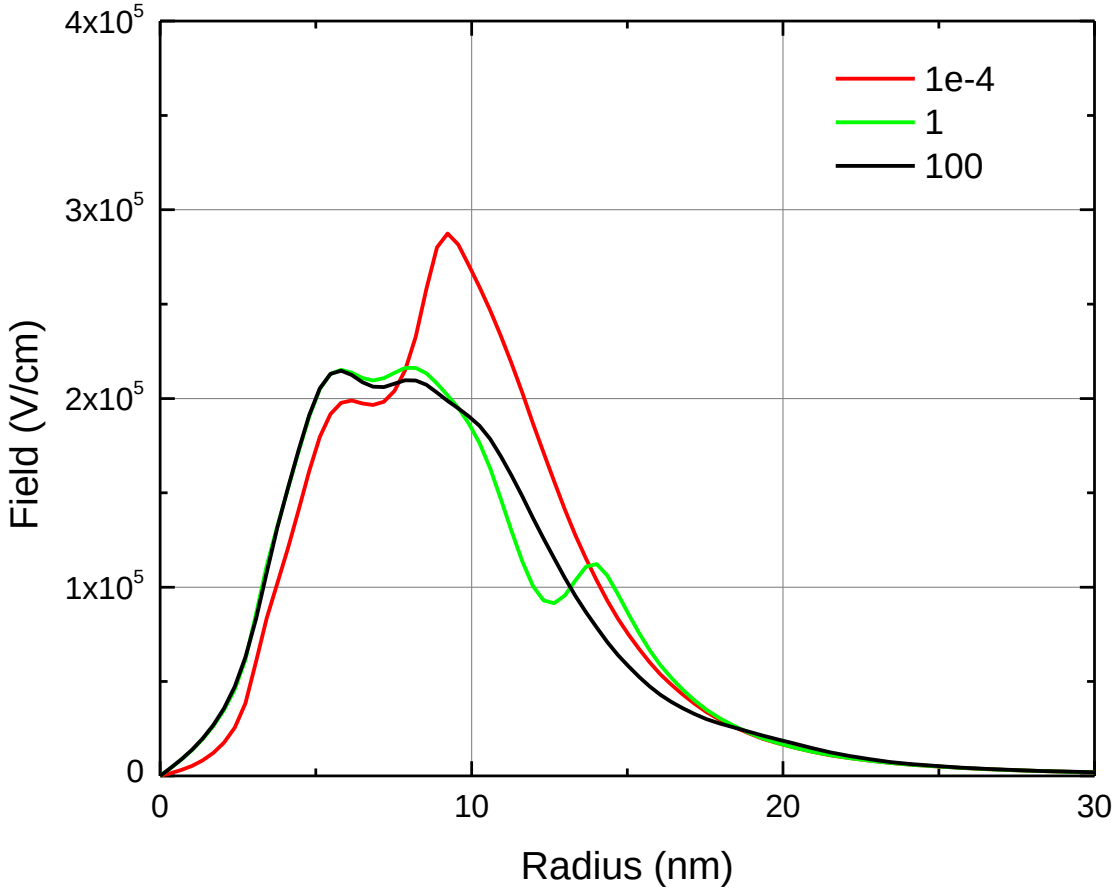

Figure 8. Electric field vs radius at various times indicated in the legend.

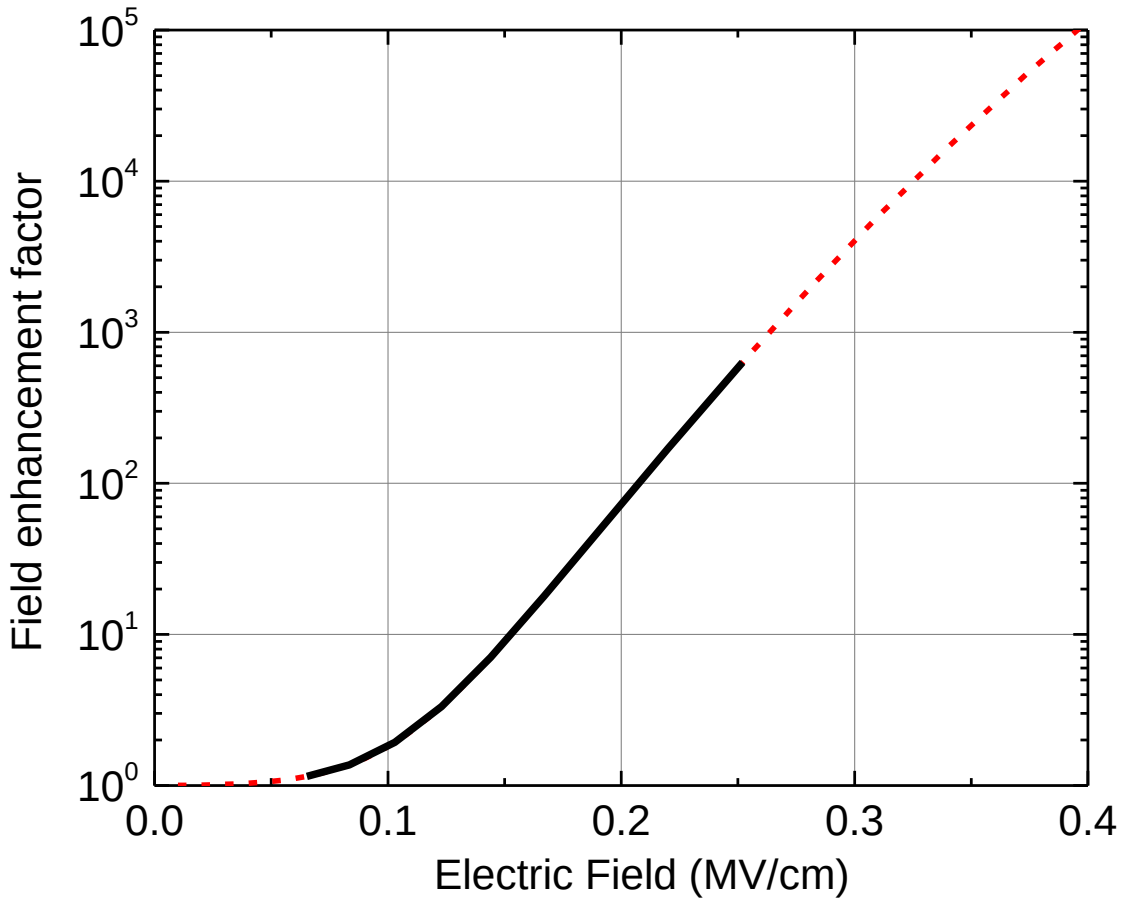

Figure 9. Calculated field-enhancement of the carrier recombination vs field strength, for the parameter values determined from the fit to data from DLTS experiments. The solid black region of the curve shows the range of values covered by the DLTS measurements. (Data provided by Robert Fleming.)

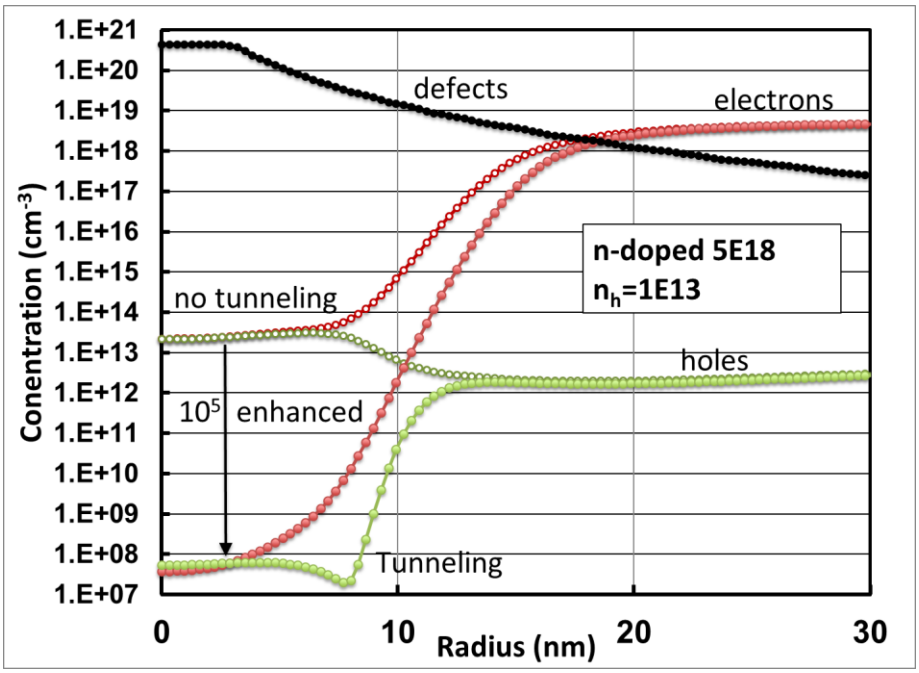

Figure 10 Carrier concentrations vs radius with (solid symbols) and without (open symbols) field-enhanced recombination from the static defect model. Black curve shows the defect concentration.

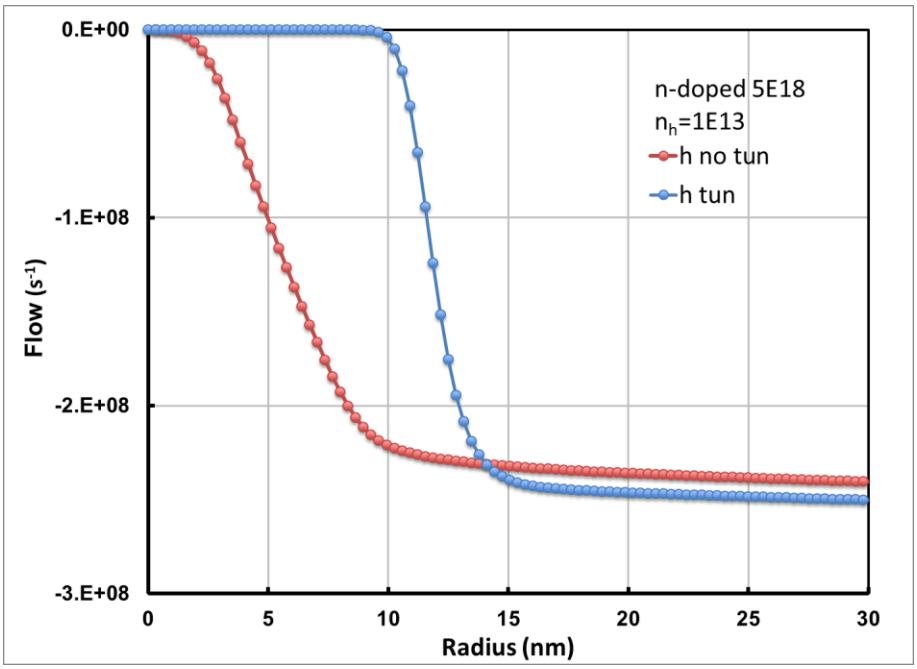

Figure 11 Carrier flow vs radius with (blue) and without (red) field-enhanced recombination from the static defect model.

DISTRIBUTION

1	MS0352	Charles Hembree	1344
1	MS1056	Jonathan Custer	1111
1	MS1146	Philip Cooper	1384
1	MS1146	Brian Hehr	1384
1	MS1177	Eric Keiter	1355
1	MS1177	Gary Hennigan	1355
1	MS1177	Joseph Castro	1355
1	MS1179	Leonard Lorence	1341
1	MS1322	Peter Schultz	1444
1	MS1415	Alan Wright	1131
1	MS0899	Technical Library	9536 (electronic copy)

Sandia National Laboratories